Results in Engineering 27 (2025) 106534

Contents lists available at ScienceDirect

Results in Engineering

journal homepage: www.sciencedirect.com/journal/results-in-engineering

Research paper

# Integrated power and attitude sensors tile for a small spacecraft

Zainab Mousawi [a], Anwar Ali [a,*], Muhammad Rizwan Mughal [b], Shoaib Ahmed Khan [c], Augustine Egwebe [a]

[a] Electronic and Electrical Engineering Department, Swansea University, Wales, United Kingdom
[b] Department of Electrical and Computer Engineering, Sultan Qaboos University (SQU), Muscat, Oman
[c] College of Electrical and Mechanical Engineering, Guangzhou University, Guangzhou, China

ARTICLE INFO

*Keywords:*
Small satellites
Power subsystem
Nano satellite
Hexagonal satellite
Power distribution bus
Power management

ABSTRACT

In pursuit of compact, redundant and miniaturized subsystems for nanosatellites, this paper introduces the design of a Hexagonal Power Management and Attitude Sensor Tile (HPMAST), a multifunctional unit integrated into an hexagon-shaped spacecraft. Six HPMAST tiles are mounted on the external periphery of the spacecraft. Each HPMAST tile combines high-efficiency solar energy harvesting, power conversion with localized maximum power point tracking (MPPT), and attitude determination capabilities within a tightly packed eight-layer PCB structure. The power subsystem features a hysteresis-controlled boost converter that raises the 19.8 V input, generated from 36 photovoltaic cells arranged as four parallel strings of nine series-connected 2.2 V cells, to a regulated 28 V Power Distribution Bus (PDB). Each HPMAST tile with dimensions 16.5 cm x 99 cm produces 36 W, with conversion and control circuitry located on the panel's backside. Embedded within four internal PCB layers is a reconfigurable planar magnetorquer coil, designed for torque generation through its interaction with the Earth's magnetic field. The tile also houses miniature attitude sensors, including a gyroscope, magnetometer, and sun sensor, enabling localized three-axis attitude sensing. While the HPMAST tile primarily manages the power harvesting, conversion, and distribution subsystems of the hexagonal-shaped spacecraft, the integration of attitude sensing and actuation ensures scalability, compactness and provides more space for the payload. Findings from this work show that the proposed system achieved stable and efficient power regulation in simulation, with the hysteresis-based MPPT boost converter delivering a regulated 28 V output and maintaining voltage ripple within 0.2 V. The system achieved a peak efficiency of 93 % under standard input conditions. The embedded magnetorquer exhibited a magnetic dipole moment of 0.415 A·m² while maintaining thermal limits in the hybrid configuration. These results validate the technical feasibility and robustness of the HPMAST tile for future in-orbit deployment. In addition to power and attitude determination systems, ongoing work will focus on the thermal and magnetic characterization of the embedded coil to support future in-orbit deployment.

*List of Abbreviations*

| | |
|---|---|
| HPMAST | Hexagonal Power Management and Attitude Sensor Tile |
| EPS | Electrical Power System |
| MPPT | Maximum Power Point Tracking |
| PCB | Printed Circuit Board |
| PDB | Power Distribution Bus |
| PDS | Power Distribution System |
| ADCS | Attitude Determination and Control Subsystem |
| LEO | Low Earth Orbit |
| CSS | Coarse Sun Sensor |
| MEMS | Micro-Electro-Mechanical Systems |
| CAN | Controller Area Network |
| TMTC | Telemetry and Telecommand |
| EMI | Electromagnetic Interference |
| ADC | Analog to Digital Converter |
| MOSFET | Metal-Oxide-Semiconductor Field-Effect-Transistor |
| GaN | Gallium Nitride |
| $V_{ds}$ | Drain-Source Voltage |
| $R_{ds(on)}$ | On-state Resistance |
| $Q_g$ | Total Gate Charge |
| $I_d$ | Continuous Drain Current |
| $R_{th(j-c)}$ | Thermal Resistance (junction-to-case) |

* Corresponding author.
*E-mail address:* anwar.ali@swansea.ac.uk (A. Ali).

https://doi.org/10.1016/j.rineng.2025.106534
Received 7 June 2025; Received in revised form 21 July 2025; Accepted 29 July 2025
Available online 30 July 2025

## 1. Introduction

CubeSats, pioneered in 1999 by Jordi Puig-Suari and Bob Twiggs, are compact satellites initially designed for Low Earth Orbit (LEO) missions focusing on remote sensing and communications [1,2],. Based on the 1 U form factor (10 cm x 10 cm x 11.35 cm, < 1.3 kg), CubeSats support modular expansions such as 2 U, 3 U, and 6 U, and enable the deployment of a wide range of mission profiles [1,2],. Since their first launch in 2003, CubeSats have revolutionized space technology, supporting applications in climate monitoring, environmental research, astronomy, global communications, and defense, including early warning systems and intelligence gathering [3–5]. Their cost-effectiveness and modularity significantly lower entry barriers to space exploration, facilitating access for universities, research institutes, and independent innovators, thereby fostering educational opportunities and hands-on experience for future aerospace professionals [6,7],. Recent CubeSat platforms have also adopted 3D-printed structural enclosures using lightweight thermoplastics to further reduce development costs and mechanical complexity, particularly for atmospheric and environmental monitoring missions [8].

However, CubeSats face critical limitations arising from their compact architecture. In particular, they have a very limited surface area for solar energy collection (often only a couple of panels receive sunlight at any given time), resulting in a meagre onboard power budget [9]. Internally, the limited volume constrains payload capacity and prevents integration of complex or high-power subsystems [10]. These constraints impose significant challenges in power management, as energy availability must be tightly allocated among competing subsystems such as communications, computing, and control electronics. Power spikes from payload operations or attitude control actuators often require careful scheduling and prioritization to avoid overloading the system. Furthermore, the limited available surface and internal space hinder the use of large batteries or advanced regulation circuits [11].

Thermal management introduces an additional layer of complexity: high-power components, such as phased-array antennas and RF amplifiers, generate significant heat that is difficult to dissipate in the absence of convective cooling [9]. This challenge is exacerbated by the miniaturization trend and increasing internal power densities in CubeSats, where thermal pathways are limited by structural design constraints [12]. Communication throughput is also affected by limitations in antenna design, as CubeSats typically rely on low-gain antennas (e.g., simple monopoles), which limit data rates and increase susceptibility to interference, while high-gain or beam-steering antennas are often unfeasible due to power and spatial limitations [9,10],. Additionally, deployable structures such as fold-out antennas and solar panels carry the risk of mechanical failure in their deployment mechanisms [10]. As a result, the limited thermal dissipation capacity becomes a core constraint in CubeSat power management, as heat accumulation can lead to performance degradation or failure, requiring tight coordination between energy generation, conversion, and consumption [10,11],.

To overcome these challenges and bridge the gap in integrated power and attitude subsystems for CubeSats, this paper presents the Hexagonal Power Management and Attitude Sensor Tile (HPMAST) as a novel integrated subsystem for distributed power management and attitude control. Each HPMAST unit combines the satellite's Electrical Power System (EPS) (solar energy collection, power conditioning, storage, and distribution) with attitude determination sensors and control components into a single modular tile. Each hexagonal-shaped spacecraft features a modular hexagonal geometry that facilitates seamless tiling around the satellite periphery and contributes to structural robustness and thermal symmetry, as depicted in Fig. 1 [12,13],. By mounting six HPMAST units around the spacecraft, this design implements a module-integrated architecture that inherently increases redundancy and reliability in power [14] and attitude control functions [15,16]. In the proposed hexagonal satellite platform (shown in Fig. 1), six identical HPMAST units are mounted at the outer periphery, one on each side of a hexagon-shaped structure. This configuration reserves the interior volume of the spacecraft for the payload, while the six surrounding HPMAST modules collectively handle all power generation and management, as well as provide attitude sensing and control for the satellite bus [16,17],. Table 1 summarises how the proposed HPMAST design addresses the main limitations of conventional CubeSat platforms.

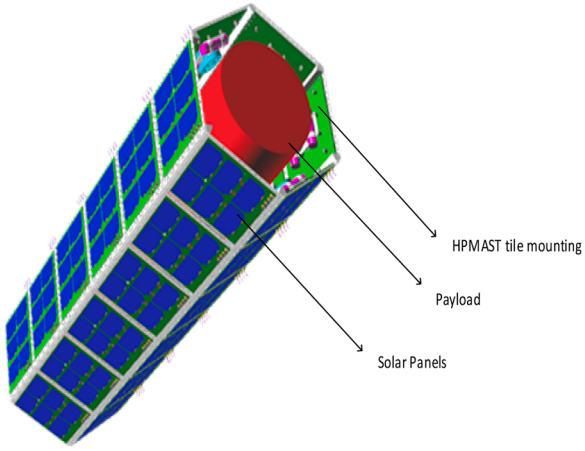


**Fig. 1.** 3D model of HPMAST-inspired small hexagonal satellite.

The HPMAST architecture employs an eight-layer PCB configuration, as illustrated in Fig. 2. It integrates three primary subsystems: power management, attitude determination, and attitude control, each distributed across specific PCB layers. The top layer incorporates a high-efficiency solar panel (16.5 cm × 99 cm) and sun sensors, which contribute to both the energy harvesting and attitude determination subsystems. Additional attitude sensors, such as magnetometers and gyroscopes, are positioned on external surfaces to provide multi-axis orientation data. Layers 2 to 5 host planar magnetorquer coils that form the core of the attitude control subsystem, generating magnetic torque without requiring external moving parts. Layers 6 and 7 act as ground planes to enhance signal integrity and mitigate Electromagnetic Interference (EMI). The bottom layer accommodates the core functional blocks, including voltage regulation, power distribution, and control drivers. By integrating these subsystems into a compact, modular structure, HPMAST enables precise attitude estimation and closed-loop control while supporting efficient onboard power regulation.

HPMAST's power management begins with body-mounted solar panels that harvest sunlight and feed it into a boost converter with Maximum Power Point Tracking (MPPT), which steps the unregulated array voltage up to a sTable 28 V main bus. This regulated bus supplies all onboard electronics through current-limited distribution circuits, while the integrated converter also handles battery charging and fault protection to ensure a reliable energy supply. Simultaneously, the tile

**Table 1**
HPMAST solutions to conventional CubeSat limitations.

| Limitation in Conventional CubeSats | How HPMAST Addresses It |
|---|---|
| 1. At zenith angle, only a single panel receive sunlight. | 1. Three tiles will receive sunlight at zenith angle. One tile will be at zenith angle (90°) and the other two tiles will be at 30° to the sunlight. |
| 2. Limited volume constrains payload capacity | 2. Integrates power and attitude systems into external tiles, freeing internal space for payload. |
| 3. Due to small size, thermal management complexity increases. | 3. Distributes heat generation across multiple tiles, enhancing radiative cooling. |
| 4. Low-gain antennas limit communication throughput | 5. Modular tile architecture accommodates multiple or higher-gain antennas without reducing payload volume. |

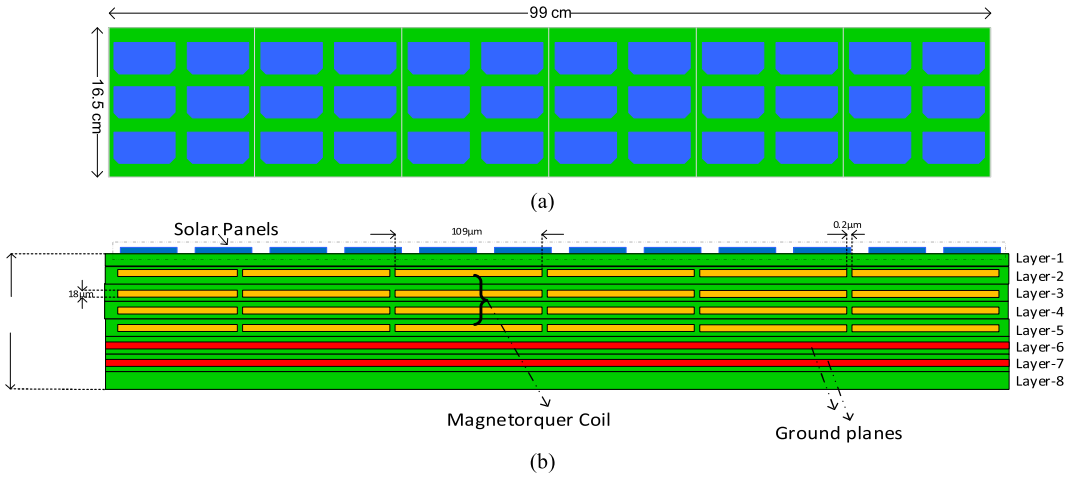


**Fig. 2.** HPMAST tile structure: (a) Top view of the photovoltaic solar array integration. (b) Cross-sectional view of the embedded magnetorquer coils and multi-layer PCB design.

incorporates a compact Attitude Determination and Control Subsystem (ADCS), featuring a suite of sensors, including a sun sensor, magnetometer, and MEMS gyroscope, that continuously estimate the satellite's three-axis orientation. These sensors are distributed around the hexagonal structure to provide wide-angle coverage of solar and geomagnetic reference vectors. Recent satellite-based sensor architectures have demonstrated that distributed multi-sensor configurations, combined with event-driven acquisition strategies, can enhance energy efficiency and fault tolerance in modular satellite platforms [18]. For actuation, a planar magnetorquer coil is embedded within the PCB layers, generating control torque through interaction with Earth's magnetic field [19]. These planar magnetorquers offer high reliability due to the absence of moving parts, low power consumption, and seamless integration within the board structure [20]. By integrating EPS and ADCS functions into a single multi-layer module, HPMAST optimizes mass and volume, with the shared PCB footprint and internalized components enabling scalable, fault-tolerant control [19]. Ultimately, this work presents HPMAST as a compact, robust, and integrated solution for power and attitude management in next-generation nanosatellite platforms. The main objective of this study is to design, implement, and evaluate the HPMAST tile as a multifunctional subsystem that integrates power conditioning, distribution, and attitude determination capabilities within a modular nanosatellite architecture. For instance, HPMAST aligns with recent developments in module-integrated Electrical Power System (EPS) architectures, which enhance CubeSat reliability and free internal volume for mission payloads [21]. It also integrates Attitude Determination and Control System (ADCS) designs utilizing embedded magnetorquers for precise attitude control in Earth observation missions [22], demonstrating its practical applicability in modern nanosatellite platforms. The paper is structured as follows: Section II presents the

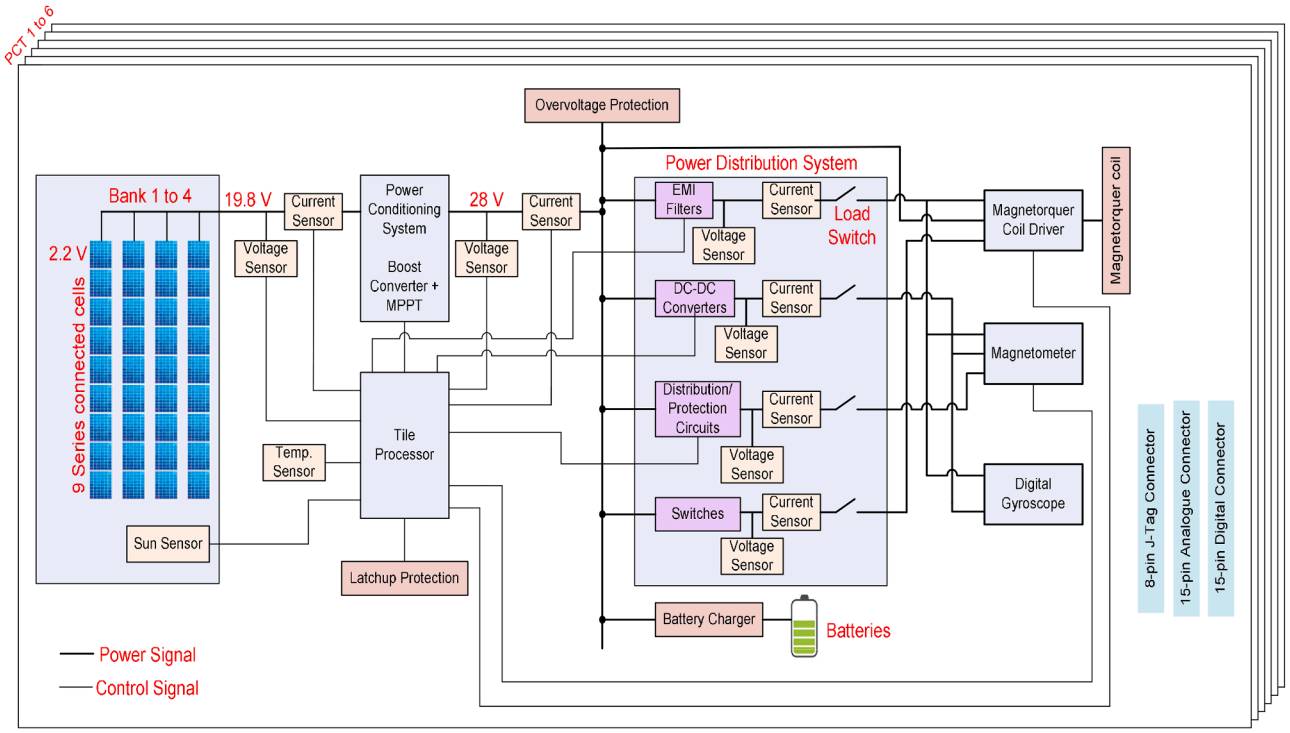


**Fig. 3.** Power conditioning system architecture in a single satellite tile.

design of the power conditioning system including the solar panel, boost converter, and hysteresis-based MPPT controller. Section III describes the power distribution system. Section IV details the attitude determination and control subsystem, covering sun sensors, magnetometers, and gyroscopes. Section V presents the embedded planar magnetorquer design. Section VI includes future work direction. Finally, Section VII concludes the paper with key findings.

## 2. Power conditioning system

The EPS of the proposed hexagonal satellite platform is designed to optimize power harvesting, regulation, and distribution within the geometric and thermal constraints of a modular tile architecture, namely the HPMAST. As shown in Fig. 3, each tile integrates a complete power conditioning and distribution chain, starting with energy harvested from photovoltaic arrays and ending with regulated delivery to critical subsystems such as the ADCS and other satellite subsystems.

The power conditioning stage serves as the EPS front end, converting the unregulated output of the solar array into a sTable 28 V DC bus using a boost converter regulated via a MPPT mechanism. Embedded telemetry components including current sensors, voltage dividers, sun sensors, and thermal monitors, continuously supervise operating conditions, while logic-level control is handled by a dedicated tile processor interfaced with latch-up and overvoltage protection circuits. The architecture clearly defines signal flows for both power and control, facilitating fault isolation and enhancing system-level observability.

The hexagonal-shaped spacecraft has six solar panels mounted on its external periphery. Each solar panel, with dimensions 16.5 cm × 99 cm, harvests solar energy of up to 36 W, enough to meet the satellite subsystem's power requirement. As shown in Fig. 4, the solar panel comprises 36 CESI CTJ-LC solar cells arranged in four parallel banks, each bank consisting of nine series-connected cells. Commercially available 1-Watt CESI CTJ-LC cells (efficiency ≈ 28 % at AM0, 25 °C; temperature coefficients $\frac{\Delta V_{OC}}{\Delta T} = -6.19\ \boldsymbol{mV/^{\circ}C}$, $\frac{\Delta I_{SC}}{\Delta T} = 0.0114\ \boldsymbol{mA/cm^2/}\ ^{\circ}C$) with 2.48–2.62 V open-circuit voltage and 0.42–0.44 A short-circuit current are used [23]. The choice of this configuration reflects a design trade-off between current and voltage to match the requirements of the boost converter input. As illustrated in Fig. 4, bypass diodes are placed across each series string to mitigate partial shading effects and ensure reliability, while a protection diode at the array output prevents reverse current during low-illumination periods.

In LEO, solar panels are subjected to partial shading, radiation damage, thermal cycling, and long-term ageing effects. These phenomena can degrade individual cell performance over time, resulting in reduced open-circuit voltage and current output within affected strings. However, the four-parallel bank configuration mitigates this impact, as degradation in one string proportionally reduces the total output without causing complete system failure [24,25],.

To further enhance reliability under both partial shading and degradation conditions, bypass diodes are placed across each series string to protect the array against severe power mismatch losses and potential hotspot formation, further enhancing the resilience of the solar power subsystem [24,25],. Additionally, a protection diode at the array output prevents reverse current flow during low-illumination conditions. This arrangement aligns with established nanosatellite solar panel design practices, where each cell is modelled by an equivalent diode to represent its I–V characteristics under MPPT and dynamic loads [26,27], and supports HPMAST best practices for modularity, fault tolerance, and long-term mission resilience.

This robust electrical foundation enables seamless integration with the HPMAST multi-layer PCB architecture, supporting downstream voltage regulation, power distribution, and attitude sensors such as magnetometers and gyroscopes, all powered directly by the EPS.

### 2.1. Boost converter

In the proposed HPMAST design, the boost converter elevates the photovoltaic (PV) array output from 19.8 V to a regulated 28 V rail, providing stable power to critical subsystems including attitude sensors, battery management units, and distributed control electronics. Its operation is based on a two-phase switching cycle: the ON state and the OFF state, as illustrated in Fig. 5, which shows the current flow and energy transfer paths within each phase. During the ON state, the switch is closed, allowing current from the photovoltaic array to flow through the inductor and build up magnetic energy [26]. In this phase, the output diode is reverse-biased, isolating the load and preventing energy from being transferred. Conversely, in the OFF state, the switch opens, and the inductor's collapsing magnetic field induces a voltage that forward-biases the output diode [26]. This enables current to flow into the output capacitor and the load, effectively stepping up the voltage. This two-phase operation is the cornerstone of step-up DC-DC boost

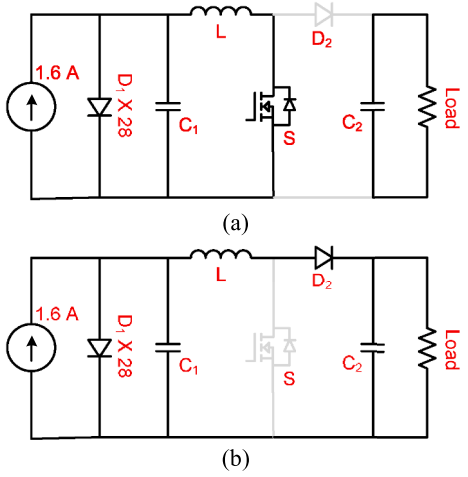


**Fig. 5.** Boost converter operation modes. (a) On-state: charging inductor. (b) Off-state: inductor discharging into load.

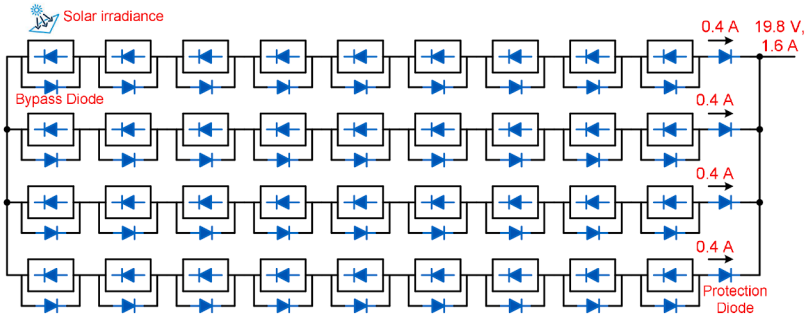


**Fig. 4.** Solar array configuration with bypass and protection diodes.A. Solar Panel.

conversion widely adopted in small satellite EPS [27].

The theoretical relationship between output voltage and duty cycle under continuous inductor current is derived from the principle of inductor volt-second balance in steady-state conditions. In an ideal boost converter operating in Continuous Conduction Mode (CCM), the energy stored in the inductor during the ON phase is fully transferred to the output during the OFF phase, leading to the following relationship:

$$V_{out} = \frac{V_{in}}{1 - D} \tag{1}$$

Where, $V_{in}$ is the input voltage from the solar array and $D$ is the duty cycle of the switching signal. This expression illustrates the nonlinear dependence of output voltage on duty cycle, emphasizing the importance of accurate duty cycle control. While Table 2 lists the nominal duty cycle as 0.3 for design calculation purposes, it should be noted that the actual duty cycle varies dynamically within the hysteresis window based on input voltage thresholds ($V_H$ and $V_L$) to maintain stable MPPT operation, rather than operating at a fixed duty cycle [28].

To ensure proper component selection and efficient operation, the following design equations are applied [29]. The minimum inductance is calculated as:

$$L_{min} = \frac{D \times V_{in}}{I_{pk} \times \Delta I_{max} \times f_{sw}} \tag{2}$$

The input and output capacitance values are determined by:

$$C_1 = \frac{D \times I_{in}}{\Delta V_{in} \times f_{sw}} \tag{3}$$

$$C_2 = \frac{D \times I_{out}}{\Delta V_{out} \times f_{sw}} \tag{4}$$

The boost converter parameters used in the design are summarized in Table 2. These values ensure that the converter meets the required power and thermal constraints. Schottky diodes and low-ESR capacitors are utilized to minimize losses and improve high-frequency performance [26].

To optimize performance, various switching devices were evaluated for the boost converter, as shown in Table 3. The Gallium Nitrate (GaN) based GAN3R2–100CBE exhibited the best characteristics, with low on-state resistance, an ultra-low gate charge of 9.2 nC, and thermal resistance ($R_{th}$) of 0.3 °C/W, ensuring a simplified gate driver circuit, higher frequency and high-efficiency operation [30]. GaN devices are next-generation switching devices and will outperform silicon-based switching devices in low-voltage applications. These parameters were prioritized to ensure low conduction and switching losses at the 25 kHz operating frequency, thereby minimizing thermal buildup and allowing for compact heat dissipation within the multi-layer PCB design. GaN devices also offer greater radiation hardness compared to traditional MOSFETs, which enhances resilience in LEO environments.

**Table 2**
Boost converter design parameters.

| Parameter | Optimal Value |
|---|---|
| Input Voltage ($V_{in}$) | 19.8 V |
| Output Voltage ($V_{out}$) | 28 V |
| Load Resistance ($R_L$) | 25 Ω |
| Input Current ($I_{in}$) | 1.6 A |
| Output Current ($I_{out}$) | 1.13 A |
| Current Ripple ($\Delta I$) | 30 %<br>(Min. to Max Value: 20–40 %) |
| Rated Power ($P$) | 31.68 W |
| Switching Frequency ($f_{sw}$) | 25 kHz |
| Duty Cycle ($D$) | 0.3 |
| Inductor Value ($L$) | 500 $\mu$H |
| Input Capacitance ($C_1$) | 22 $\mu$F |
| Output Capacitance ($C_2$) | 22 $\mu$F |
| On-Time Duration ($T_{ON}$) | 12 $\mu$s |

**Table 3**
Possible switching devices for the HPMAST Boost Converter.

| Type Number | $V_{DS}$ (V) | $R_{DS(on)}$, (mΩ) | $Q_G$ (nC) | $I_D$ (A) | $R_{th}$ (j-c) ( °C /W) |
|---|---|---|---|---|---|
| IPD033N06N | 60 | 3.3 | 38 | 90 | 1.4 |
| SiJ188DP | 60 | 3.85 | 22 | 92 | 1.9 |
| BSZ040N06LS5 | 60 | 4.0 | 18 | 101 | 1.8 |
| GAN3R2–100CBE | 100 | 2.4 | 9.2 | 60 | 0.3 |

A complete schematic of the boost converter with MPPT technique is presented in Fig. 6. The simulation, conducted in LTspice, models 36 series-connected solar cells using ideal diodes to replicate the 2.2 V per-cell output, with a current source supplying 1.6 A to represent the total array output. The LT1017 comparator governs MOSFET switching through a reference voltage set by a resistive divider, ensuring stable and responsive control while optimizing power extraction via MPPT [31].

### 2.2. Hysteresis-Based MPPT controller

The proposed MPPT circuit employs an analogue hysteresis control strategy, selected for its simplicity, fast transient response, and inherent robustness in space-constrained, radiation-prone environments typical of CubeSat missions [29]. In contrast to digital approaches such as Perturb and Observe (P&O) or Incremental Conductance (IC), the hysteresis method eliminates the need for analogue-to-digital converters (ADCs), Pulse Width Modulation (PWM) modules, and complex software routines, thereby reducing overall power consumption and enhancing fault tolerance [28].

Fig. 6 shows the proposed simulation circuit for the solar panel, boost converter and the MPPT controller. As solar panel is a constant current source, therefore the simulation circuit is composed of a current source, series connected diodes (36) and a parallel capacitor. The converter is a simple boost converter while the hysteresis controller is implemented using an LT1017 comparator and a voltage divider network composing of resistors $R_1$, $R_2$, and $R_3$ (Fig. 6). In nominal operating conditions the solar panel output will be around 19.8 ± 2 V. Therefore, we have chosen nominal output voltage 19.8 V resulting in an upper threshold ($V_H$) limit of 20.8 V and lower threshold ($V_L$) of 18.8 V. The MOSFET switching is

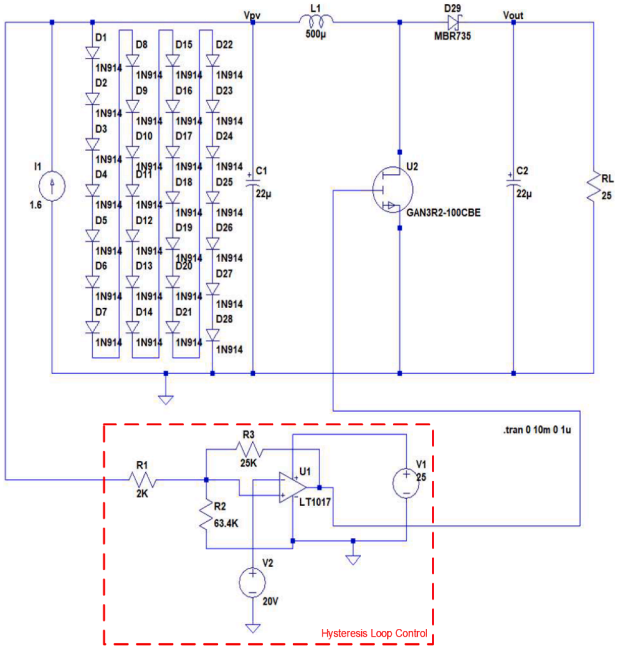


**Fig. 6.** Proposed boost converter circuit with hysteresis-based MPPT control logic.

controlled through the hysteresis loop controller. Let start from the initial condition when the MOSFET is off. The current source will charging the capacitor and the voltage of the capacitor will rise to the upper threshold, $V_H = 20.8$ V. According to the design, the hysteretic loop controller will turn on the MOSFET switch at $V_H$ voltage level and the capacitor will start discharging. When the capacitor voltage decreases to lower threshold, $V_L$=18.8 V, the hysteretic loop controller will turn off the MOSFET and the capacitor voltage will start increasing and will reach to upper threshold VH=20.8 V and the cycle will repeat [28]. The voltage difference between these two thresholds defines the hysteresis band (HB), which is expressed as:

$$\Delta V_{HB} = V_H - V_L \tag{5}$$

This approach maintains the converter's input close to the maximum power point with minimal hardware complexity. With a fixed $R_3 = 25$ kΩ and a supply voltage $V_{CC} = 25$ V, $R_1$ is calculated as 2 kΩ using:

$$R_1 = R_3 \left[\frac{V_{HB}}{V_{CC}}\right] \tag{6}$$

The reference voltage (Vref) of 18 V is selected to fall within the hysteresis band defined by the comparator thresholds. To ensure correct switching, Vref must be lower than the upper threshold (VH) and higher than the lower threshold (VL), satisfying the following condition [28]:

$$V_H > V_{ref}\left(1 + \frac{V_{HB}}{V_{CC}}\right) \tag{7}$$

Where, $V_{HB}$ is the hysteresis band (2 V), and $V_{CC}$ is the supply voltage (25 V). Setting $V_{ref}$ to 18 V ensures this condition is met, enabling stable switching without false triggering, which is critical for reliable MPPT operation in the boost converter.

A load resistor ($R_L = 25$ Ω) is connected at the output of the converter, as illustrated in Fig. 6, to represent the average power demand of the satellite subsystem. To maintain this constraint, $R_2$ is obtained using the following equation [28]:

$$R_2 = \left[\left(\frac{V_H}{V_{ref} * R_1}\right) - \frac{1}{R_1} - \frac{1}{R_3}\right]^{-1} \tag{8}$$

Substituting the known values, the final value of $R_2$ was chosen as 63.4 kΩ, aligning with the design constraint and ensuring correct hysteresis window operation.

### 2.3. Tile processor unit

Each HPMAST tile integrates a dedicated Tile Processor Unit responsible for managing local power conditioning and telemetry acquisition. The Tile Processor oversees the operation of the boost converter and the hysteresis-based MPPT controller, ensuring that maximum power is harvested from the photovoltaic arrays under varying illumination conditions. It continuously monitors critical parameters, including input and output voltages, currents, and tile surface temperature, and manages the switching logic of the converter accordingly. It also executes local fault detection and isolation tasks for its power conditioning circuits, enhancing overall system reliability at the tile level.

In addition to power regulation, the Tile Processor interfaces with onboard sensors such as the sun sensor to provide localized telemetry data. This data is communicated to the satellite's central On-Board Computer (OBC) via CAN bus or telemetry lines for system-level integration and health monitoring, while telecommand instructions from the OBC are received to update operational modes and control logic as needed.

Importantly, while the Tile Processor manages power conditioning and telemetry within its own tile, the overall satellite power distribution is handled by the Power Distribution Unit (PDU), which is controlled by a central microcontroller. The tile processor is a commercial off-the-shelf (COTS) TI MSP430F5438A [28,32], which details are given in PDM section. This hierarchical approach allows each HPMAST tile to function autonomously for energy harvesting and conditioning while delegating the final power switching and distribution decisions to the Power Distribution System (PDS) section to ensure optimal load management across the entire satellite.

### 2.4. Results and analysis

The performance of the proposed boost converter under hysteresis-based MPPT control is evaluated through both output voltage and load current waveforms, as presented in Fig. 7(a) and Fig. 7(b). These results simultaneously cover two input scenarios: nominal input condition (19.8 V) and variable input condition (18–21 V), providing a comprehensive assessment of the converter's dynamic and steady-state performance under realistic photovoltaic fluctuations.

In Fig. 7(a), the output voltage response of the DC-DC boost converter is shown. Under the nominal condition, the output voltage rapidly rises to its steady-state value of approximately 28 V within 2 ms, demonstrating fast transient response and good dynamic behavior. Throughout the simulation, the voltage remains stable with minimal ripple (~0.2 V peak-to-peak), ensuring reliable power delivery to satellite subsystems. Under variable input conditions (18–21 V), despite fluctuations at the input side, the converter effectively maintains a regulated output at 28 V, evidencing the robustness of the hysteresis-based MPPT controller. The ability to sustain output voltage stability under variable inputs highlights the controller's adaptability and resilience to environmental changes typically encountered in orbit.

Similarly, Fig. 7(b) presents the load current response. In both nominal and variable input conditions, the output current reaches approximately 1.17 A and follows a comparable transient profile to the voltage. The current ripple remains small and within acceptable limits across both scenarios, confirming efficient energy transfer and minimal switching losses even during input perturbations.

The converter achieved an overall efficiency of approximately 93 %, calculated from output power (29 V × 1.17 A) over input power (22.8 *V* × 1.6 A). Voltage ripple was consistently maintained at ~0.2 V, representing 0.71 % of the nominal output voltage. Measurement uncertainty was estimated at ±0.05 V for voltage and ±0.03 A for current, considering component tolerances (shunt resistor accuracy, capacitor ESR) and LTspice model characteristics. These metrics collectively validate the converter's reliable and efficient performance under both steady-state and dynamic input conditions.

Together, these results confirm that the hysteresis-controlled boost converter achieves stable output regulation, low ripple, and fast response time, all of which are key performance criteria for nanosatellite EPS operating in dynamic orbital environments. To further validate these findings, Table 4 presents a comparative analysis with existing CubeSat EPS boost converter designs reported in [19,28],.

Compared to the boost converter using constant voltage MPPT control in [28], which delivers ~2.5 W output power at ~14–16 V with high efficiency (~93 %), and the interleaved boost converter in [19], which delivers 13.4 W at 14 V with a similar ~93 % efficiency, the proposed HPMAST also achieves an efficiency of approximately 93 %, matching the performance of recent designs.

However, HPMAST delivers a regulated 28 V output and 36.48 W power, outperforming typical CubeSat subsystem bus-level voltage requirements (commonly 12–14 V [28]), while the available output power is sufficient to support all the subsystems along with the communication payloads, which generally range from ~10 W for basic telemetry modules up to ~20–50 W for higher data rate transmitters in larger CubeSats (e.g., 6U–12 U platforms) [32]. These experimental results align with the theoretical design calculations (Sections II.B and II.C), where the duty cycle (nominal 0.3), inductor (500 μH), and capacitor sizing were optimized to minimize output ripple (~0.2 V) and switching losses, ensuring efficient and stable operation. This confirms that the proposed

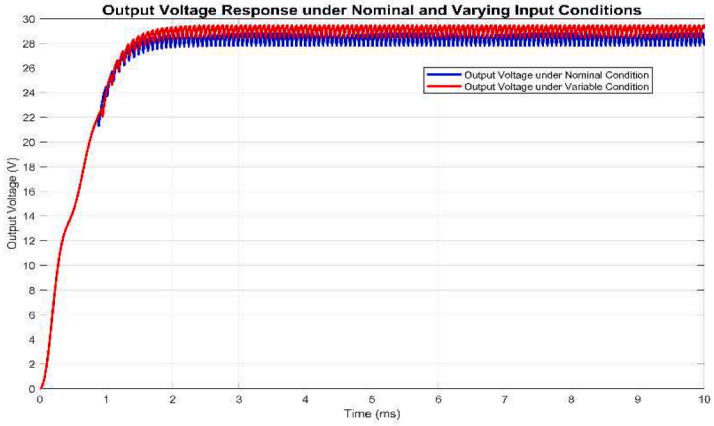


(a) Output voltage of the dc-dc boost converter.

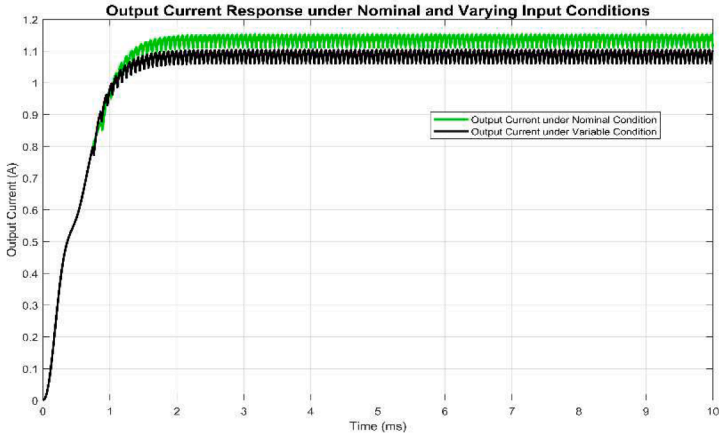


(b) Load current of the dc-dc boost converter.

**Fig. 7.** LTSpice Simulation results of photovoltaic-powered boost converters with MPPT under nominal and varying input conditions.

**Table 4**
Comparison of proposed converter with existing CubeSat designs.

| Study | Converter Type | Control Method | Efficiency ( %) | Output Ripple (V) | Rated Output Voltage (V) | Output Power (W) | Overall Losses ( %) |
|---|---|---|---|---|---|---|---|
| **HPMAST** | Boost Converter | Hysteresis-based MPPT Controller | ~ 93 % | ~ 0.2 V | 28 V | 30.8 W | 10.3 % |
| [19] | Interleaved Boost Converter | MPPT Constant Voltage with hysteresis window | ~ 93 % | ~ 0.28 V | 14 V | 13.4 W | 7 % |
| [28] | Boost Converter | MPPT Constant Voltage | ~ 93 % | < 0.25 V (est.) from Fig. 7b [28] | ~14 –16 V | ~ 2.5 W (est.) | ~ 2.4 % (est.) |

architecture achieves state-of-the-art efficiency comparable to recent CubeSat converters [19,28], while offering superior voltage and power capabilities, demonstrating its practical viability in high-demand nanosatellite missions.

## 3. Power distribution system

The HPMAST platform employs a highly modular, fault-tolerant, and scalable power distribution architecture to support its multi-tile design. Each tile hosts an independent Power Distribution Module (PDM) that handles input voltage regulation, current sensing, load switching, and telemetry, ensuring reliable operation under dynamic and constrained conditions characteristic of distributed small satellite architectures such as the hexagonal HPMAST platform.

Each tile receives power via two redundant 28 V input lines originating from the Power Conditioning Module (PCM). These lines are routed through sense resistors (R1 and R3) and monitored using INA168 current sensors, which convert the sensed current to a proportional voltage using the relation:

$$V_{OUT} = (I_s)(R_{sense})(g_m)(R_{Load}) \tag{9}$$

Where, $I_s$ the sensed current, $R_{sense}$ is the sense resistor, $g_m = 200$ μA/V is the transconductance of the INA168, and $R_{Load}$ is the load resistor [33]. Voltage telemetry is acquired using voltage dividers scaled to match the MSP430 ADC input range (0–2.5 V), with filtering applied using low-pass RC networks to suppress noise [34,35],.

Power is distributed through three voltage rails: a primary 28 V line, and two regulated lines at 5 V and 3.3 V. Each rail supports both switchable and non-switchable outputs, as shown in Table 5. The 28 V bus supplies up to nine switchable lines (500 mA each), which are directly used by high-voltage subsystems. Secondary voltage rails are derived via dual-redundant LM2679S-ADJ switching regulators per rail, operating at 260 kHz with over 90 % efficiency [36,35],. The output voltage is defined by the feedback network as:

**Table 5**
Regulated power lines and their switchability in the HPMAST tile.

| Output Voltage | Number of outputs lines | Max. Current per line | Switching Capability |
|---|---|---|---|
| 28 V | 9 lines | 500 mA | Switchable |
| 5 V | 4 lines | 400 mA | Non-Switchable |
| 5 V | 5 lines | 200 mA | Switchable |
| 3.3 V | 12 lines | 500 mA | Switchable |
| 3.3 V | 8 lines | 400 mA | Non-Switchable |

$$V_{out} = V_{FB}\left(1 + \frac{R_{36}}{R_{41}}\right) \tag{10}$$

Where, $V_{FB}$ is typically 1.21 V [35].

The 5 V redundant regulator block, illustrated in Fig. 8, produces 5 V across 4 non-switchable lines (each protected by 400 mA fuses, totaling 1600 mA) and five switchable lines (each rated at 200 mA, totaling 1000 mA). Similarly, the 3.3 V redundant regulator block generates 3.3 V for a total of 20 lines: 8 non-switchable lines protected by 400 mA fuses (totaling 1600 mA) and 12 switchable lines monitored via INA168 sensors (totaling 2000 mA). The total current demands of 2600 mA for the 5 V rail and 3600 mA for the 3.3 V rail are well within the 5 A maximum output capability of the LM2679S-ADJ regulators. The implementation of dual redundant regulators for each voltage rail enhances system robustness by ensuring continuous operation even in the event of a regulator failure.

Load switching is achieved using MOSFET-based high-side switches controlled by the PDM's onboard microcontroller. Each switchable line includes a current sensor (INA168) and is actively monitored [35]. In the event of an overcurrent, the MSP430F5438A controller autonomously disconnects the affected line, implementing real-time fault isolation and enabling software-controlled power cycling of individual subsystems. Overcurrent events are detected based on a preset current threshold sustained for over 50 ms, after which the system performs a timed reconnection attempt following a 500 ms delay. If the fault persists, the line is latched off and flagged through the Controller Area Network (CAN) telemetry stream, supporting safe fault handling and remote diagnostics. Non-switchable lines are protected using fast-blow or resettable polyfuses, ensuring baseline protection even in the absence of active switching control.

The controller used is a COTS TI MSP430F5438A, a 16-bit RISC microcontroller with ultra-low power consumption and support for seven low-power modes (one active plus six progressively deeper sleep states) [34,35],. It includes automatic wake-on-interrupt behaviour and automatic return to the selected low-power mode after servicing each event. The controller features redundant SPI/I2C/CAN/UART interfaces, JTAG for in-circuit programming, and eleven general-purpose digital I/Os mapped to PDM control lines [35]. The MSP430 oversees all telemetry, load management, and latch-up protection mechanisms. It is supported by an external 32.768 kHz low-frequency crystal oscillator (ABS13 series, load capacitance 12.5 pF, operating range 40 °C to +85 °C) to provide stable timing for system operations [34], and a TPL5010 watchdog timer circuit that ensures automatic recovery from firmware hangs, as a back-up Latch-up protection or unexpected behaviour by resetting the microcontroller when necessary [37]. In addition to the Watch-dog timer SEL protection, the MSP430 itself is protected by a dedicated latch-up circuit using external MOSFETs and a timing network that disconnects its 3.3 V supply upon detection, ensuring safe power cycling and recovery, as shown in Fig. 8.

Each PDM includes a dual-channel CAN interface for robust communication with the On-Board Computer (OBC). The CAN interface is implemented using MCP2515 standalone CAN controllers and

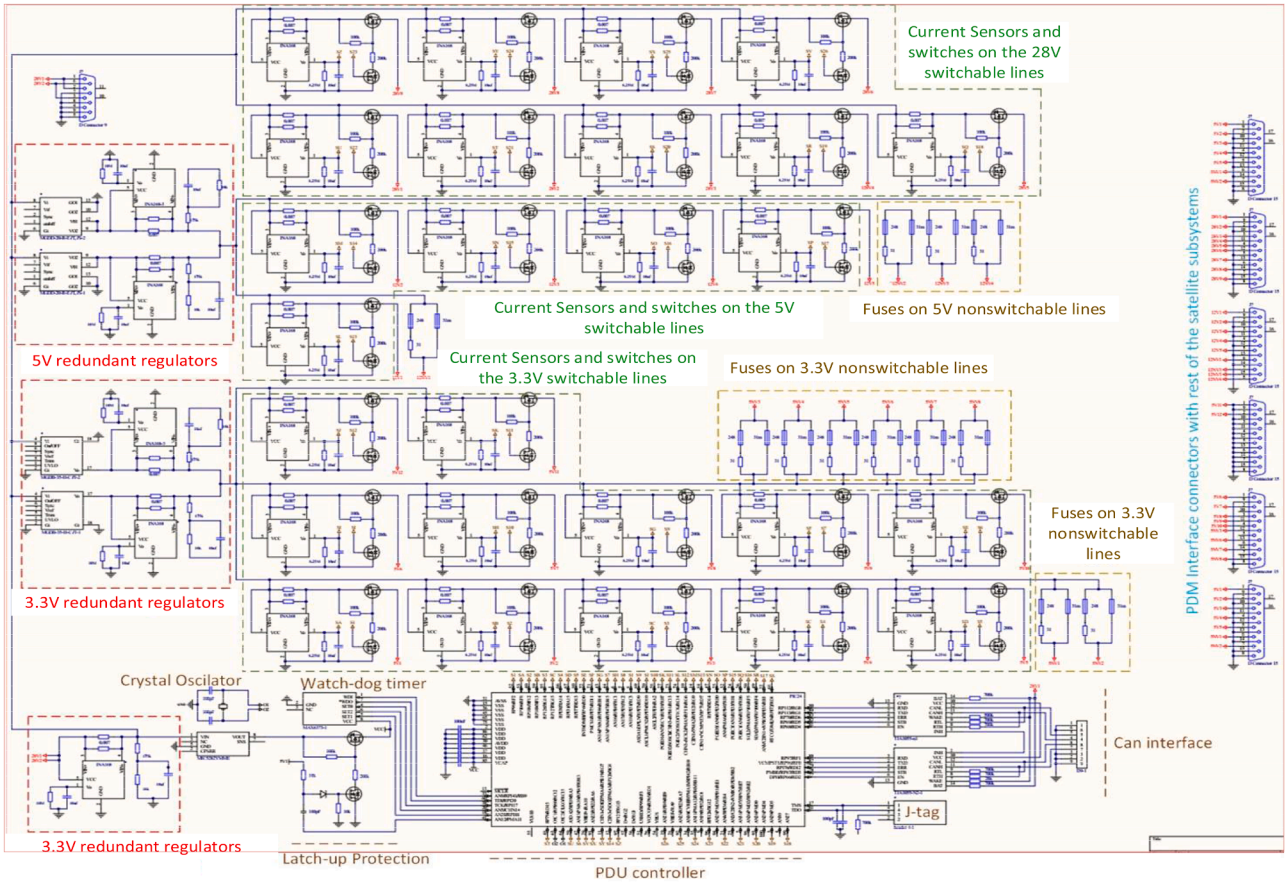


**Fig. 8.** Schematic diagram of the HPMAST tile's Power Distribution Module (PDM).

SN65HVD230D transceivers [38,39],. The MCP2515 communicates with the MSP430 via Serial Peripheral Interface (SPI) and manages CAN frame processing, while the SN65HVD230D handles bus-level signalling. Each CAN line is slope-controlled using a 10 kΩ resistor to reduce EMI, with standard 120 Ω termination [39]. The MCP2515 follows the CAN 2.0B protocol and supports both standard (11-bit) and extended (29-bit) frame formats [38]. Each message includes a Cyclic Redundancy Check (CRC) and acknowledgement field for error detection, and automatic retransmission is enabled for lost or corrupted frames [38]. A bus speed of 250 kbps was selected as a trade-off between communication robustness and EMI resilience, in line with typical CubeSat subsystem requirements. This speed ensures reliable data delivery with low bit error rates and minimal susceptibility to signal reflections across short intra-satellite wiring. Arbitration, error passive states, and bit stuffing are internally handled by the MCP2515 logic to maintain consistent communication under load. In addition to the use of internal ground planes on layers 6 and 7, EMC mitigation is achieved through multiple strategies:

1) Slope-controlled CAN transceivers reduce radiated emissions [39];
2) RC low-pass filters are applied to ADC input lines to suppress high-frequency noise [38];
3) Critical traces are routed orthogonally between adjacent layers to minimize crosstalk; and
4) Switching regulators and high-speed digital lines are shielded from EMI via-stitching around sensitive areas.

Together, these design strategies enhance the electromagnetic compatibility (EMC) of the HPMAST PDM.

To facilitate both automated and manual command pathways, the system incorporates two Telemetry and Telecommand (TMTC) interfaces: an indirect TMTC path via the controller, and a direct TMTC path accessible externally. The Direct TMTC Interface, implemented through a hardwired analog/digital access port, provides backup control over critical power switches, enabling operators to manually override automated control logic in the event of a controller malfunction or CAN bus communication failure, thus enhancing mission reliability [35].

Through this integrated architecture, the HPMAST tile's PDM achieves modular, reliable, and intelligent power distribution tailored for the stringent constraints and dynamic operating conditions of nano-satellite missions. Compared to existing micro-satellite PDM architectures [35], HPMAST integrates several important enhancements summarized in Table 6. While both designs utilize dual-redundant LM2679 switching regulators to achieve high efficiency and fault tolerance, HPMAST adopts a fully regulated ±28 V main bus rather than the unregulated ±6 V variation reported in [35], providing more stable voltage delivery to sensitive subsystems. Additionally, HPMAST includes a dedicated regulated 3.3 V rail, which enhances compatibility with modern low-voltage digital electronics, a feature not implemented in the compared design.

Moreover, HPMAST incorporates per-line current sensing using INA168 sensors, enabling precise real-time monitoring of each switchable output for improved fault detection and subsystem diagnostics, whereas [35] uses only overall bus current sensing. The use of high-side MOSFET switches controlled by the MSP430 microcontroller allows individual fault isolation and autonomous power cycling, thereby enhancing operational resilience and reliability. Finally, the integration of a direct TMTC backup interface provides additional operational security by allowing manual override of power switching in the event of controller failure or CAN bus communication loss, further supporting mission safety alongside the redundancy measures reported in [35].

**Table 6**
Key Design Feature Comparisons between HPMAST PDM and [35].

| Feature | HPMAST PDM | Design in [35] | Importance for HPMAST Design |
|---|---|---|---|
| **1. Main Bus Regulation** | ± 28 V Regulated | 28 ± 6 V Unregulated | Ensures stable voltage delivery to all subsystems, eliminates fluctuations and enhances power quality for sensitive payloads. |
| **2. 3.3 V Rail Inclusion** | • Included | • Not Included | Provides a dedicated regulated 3.3 V supply required by modern digital electronics and sensors, eliminating the need for local voltage regulation, thus improving power efficiency and thermal management. |
| **3. Per-Line Current Sensing (INA168)** | • Each switchable line is monitored | • Only overall bus sensing | Enables precise real-time monitoring of each switchable line, allowing accurate fault detection, current telemetry, and subsystem health diagnostics. |
| **4. Per-Line Fault Isolation & Power Cycling** | • Via MSP430 + MOSFET switching | • Centralized protection only | Allows individual faulty subsystems to be disconnected and reset without affecting other lines, enhancing system reliability and fault tolerance. |
| **5. Direct TMTC Backup Interface** | • Implemented | • Not Implemented | Provides manual override capability for critical power switching in case of microcontroller failure or CAN bus communication loss, improving mission safety and operational resilience. |

## 4. Attitude determination and control subsystem (ADCS)

The ADCS integrates a triad of attitude sensors: a sun sensor, a magnetometer, and a gyroscope. This combination, known as sensor fusion, provides robust and accurate orientation data under diverse lighting and magnetic field conditions encountered in LEO. By leveraging each other's strengths, these sensors together guarantee reliable and continuous attitude estimation throughout the mission. Moreover, the satellite's hexagonal structure enhances the spatial arrangement of the sensors, allowing the sun sensor and magnetometer to be mounted on orthogonal planes with wide fields of view, which improves both directionality and angular resolution. The sensor distribution, tailored to the hexagonal geometry, is summarized in Table 7.

### 4.1. Sun sensors

In small satellites, sun sensors estimate the direction of the Sun relative to the satellite's body frame, providing the sun vector as a critical input for orientation determination. In this satellite design, a Coarse Sun Sensor (CSS) is adopted due to its simplicity, compact size, low power requirements, and ease of integration. The CSS is

**Table 7**
Sensor Distribution Across Hexagonal Satellite.

| Type of Attitude Sensors | X-axis | Y-axis | Z-axis |
|---|---|---|---|
| Sun Sensor | 2 | 2 | 2 |
| Magnetometer | 2 | 2 | 4 |
| Gyroscope | 0 | 2 | 2 |

implemented using a CPC1822 photovoltaic solar cell, a compact COTS component engineered to detect both natural sunlight and artificial illumination. The output voltage of the cell increases in proportion to the cosine of the angle between the incident light and the sensor's surface normal, as illustrated in Fig. 9, and is mathematically expressed as [28]:

$$V_o = V_{max} \cos \theta \tag{11}$$

Where $V_o$ is the output voltage, $V_{max} = 1.65\ V \pm 20\%$ and $\theta$ incident angle of sunlight with respect to the normal vector of the sensor's surface [28]. Alternatively, fine sun sensors such as the MAUS Sun Sensor, offer higher angular resolution, digital output, and radiation resistance. However, their requirements for dedicated processing circuitry, increased power budget, and larger mounting area make them less suitable for HPMAST's miniaturized and power-constrained platform.

The CPC1822 outputs are digitized and processed to reconstruct the solar vector in real-time for attitude estimation. Leveraging the hexagonal geometry, the sun sensors are mounted on all six lateral facets, allowing for an unobstructed field of view and enhanced solar vector acquisition during orbital transitions, as summarized in Table 7 (two on the X-axis, two on the Y-axis, and two on the Z-axis).

To ensure compatibility with the onboard electronics, the analog output of the CPC1822 cell is regulated using a series resistor, scaling the voltage to the input range of the Analog-to-Digital Converter (ADC), which operates between 0 V and 2.5 V [28,40],. Internally, the CPC1822N device integrates multiple photodiodes in a compact SOIC-8 footprint, enhancing the output stability under varying light conditions without the need for external amplification circuitry as shown in Fig. 10. During laboratory testing, the sun sensor demonstrated a short-circuit current of 75 μA and an open-circuit voltage of 4.75 V, confirming its responsiveness and stability under various illumination levels [28].

From a system integration perspective, the sun sensor is mounted on the top surface of the HPMAST tile on the solar panel side to minimize electromagnetic interference and optimize performance for both energy harvesting and attitude sensing functions. Despite their advantages, CSS have limitations. They are restricted during eclipse periods or when obstructed by the satellite's structural elements. Their accuracy may also be influenced by environmental factors such as thermal variations or reflected light from the Earth (albedo). Moreover, CSS alone cannot provide complete three-axis attitude knowledge, particularly lacking information about yaw around the sun vector. Therefore, they are complemented with additional sensors, such as a magnetometer and a gyroscope.

### 4.2. Magnetometers

Magnetometers measure the geomagnetic field and provide critical data for onboard attitude determination algorithms in spacecraft systems. Over the years, magnetic sensor technologies have advanced significantly, driven by diverse demands across the automotive, aerospace, mobile communications, and medical industries. Magnetic sensors are classified based on operational principles and performance attributes, with the most prevalent types for geomagnetic applications being Anisotropic Magnetoresistance (AMR), Fluxgate (FG), Giant Magnetoresistance (GMR), Tunnel Magneto Resistance (TMR), Magneto-Impedance (MI), and MEMS-based sensors.

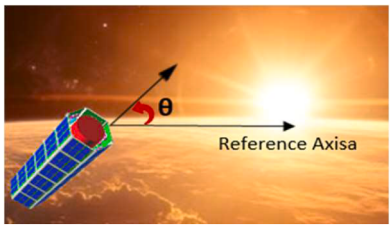


**Fig. 9.** Sun sensor angle of incidence and reference axis for attitude estimation.

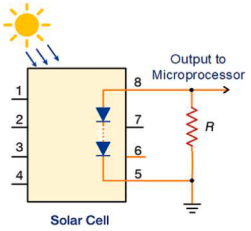


**Fig. 10.** CPC1822 solar cell interface to ADC input.

Fluxgate magnetometers, although offering high precision across a wide dynamic range (up to 764,000 nT), are constrained by their high-power consumption (~2 W) and significant mass (~500 mg), rendering them impractical for tightly integrated CubeSat designs [41,42],. GMR sensors provide excellent sensitivity and repeatability; however, their substantial hysteresis (up to 10 %) compromises their reliability in low-field environments [43]. TMR sensors outperform others in terms of sensitivity and resolution yet remain largely inaccessible due to their limited commercial availability [44]. In contrast, AMR sensors offer a mature, reliable, and low-cost solution, having been extensively adopted in the automotive and mobile sectors [45]. The Honeywell HMC105x series, particularly the HMC1053 model, exemplifies this maturity, combining a wide dynamic range (up to hundreds of milliTeslas) with nanoscale resolution capabilities [46]. A summary of magnetometer types, their inherent limitations, and mitigation strategies for CubeSat applications is presented in Table 8.

To capitalize on these advantages, the HPMAST design adopts the Honeywell HMC1053, a three-axis magnetic sensor. The HMC1053 utilizes AMR technology, optimized for low magnetic field measurements between ±2 Gauss (G) [46]. This device is integrated into the subsystem shown in Fig. 11, which includes a magnetic sensor block, a set/reset circuitry, and a signal conditioning stage [46]. The set/reset circuitry is essential for restoring the magnetic domain alignment of the HMC1053 sensor. Over time, exposure to Earth's magnetic field or strong interference can cause residual magnetization and offset drift, which degrade measurement accuracy. To address this, short, high-current pulses are applied to the on-chip set/reset straps, aligning the magnetic domains to a known reference state. According to the Honeywell datasheet, these pulses should be applied periodically during operation to ensure consistent sensor performance and to minimize the effects of hysteresis and thermal variation [46]. This process is further supported in HPMAST ADCS implementations, where set/reset pulses are used to refresh sensor sensitivity under the influence of ambient magnetic environments [28].

The raw output from the HMC1053 magnetometer consists of analogue voltages generated by three Wheatstone bridges corresponding to the X, Y, and Z axes. These voltages must be converted, conditioned, and aligned with the spacecraft's reference frame before being used in attitude estimation. These voltages must undergo differential amplification, offset correction, and frame alignment before they can be utilized in the spacecraft's attitude estimation process. The following equations present the complete signal conditioning chain from initial voltage sensing to digital calibration and coordinate transformation used to derive accurate magnetic field vectors for fusion with other attitude sensors [28]:

$$\begin{aligned} V_A &= OUT_{A+} - OUT_{A-} \\ V_B &= OUT_{B+} - OUT_{B-} \\ V_C &= OUT_{C+} - OUT_{C-} \end{aligned} \tag{12}$$

$V_A = OUT_{A+} - V_B = OUT_{B+}\ V_C = OUT_{C+}$ where $V_A$, $V_B$ *and* $V_C$ represent the differential output voltages of the three Wheatstone bridges corresponding to the X, Y, and Z axes, respectively. Since the bridges share identical characteristics, the output voltage for each axis can be expressed as [28]:

**Table 8**
Magnetometer Types, Limitations, and Mitigation Strategies in CubeSat Applications.

| Magnetometer Type | Limitations | Mitigation Strategy | Flight Implementation Example |
|---|---|---|---|
| Fluxgate (FGM) | • Drift due to temperature changes, material aging and hysteresis [41]. | • Periodic calibration (especially in-flight) [41].<br>• Hybridisation using scalar atomic sensors for auto-calibration to counter drift [41].<br>• Miniaturization (SWaP reduction) [41]. | • Dellingr CubeSat [41].<br>• SPORT mission (Scintillation Prediction Observations Research Task) [41].<br>• Gateway HERMES (uses both FGMs and magneto-inductive sensors for magnetic noise subtraction) [41]. |
| Hall-effect | • Lower sensitivity and limited accuracy, especially in low-field measurements [43].<br>• Internal electronic noise affects equivalent magnetic noise (EMN), which is a challenge in precision applications [43]. | • Integration with Magnetic Flux Concentrators (MFCs) [43].<br>• Optimization via Finite Element Method (FEM) [43]. | • Used in basic CubeSat ADCS systems and high-field applications [41, 43],. |
| Magneto-inductive (e.g. RM3100) | • Vulnerable to internal EMI originating from onboard electronics [47].<br>• Moderate noise [47]. | • Signal averaging to reduce random noise [47].<br>• Magnetic shielding during testing (e.g., copper room, shield can) [47].<br>• Increasing cycle count to improve resolution (oversampling)<br>• Development of multi-sensor configurations (e.g., multiple RM3100 units on one board) to reduce noise via data fusion [47]. | • MicroMag3 (predecessor of RM3100) flown on RAX CubeSat for attitude determination [47].<br>• Multi-sensor version of RM3100 under development-pending flight [47]. |
| Optically pumped / Proton-precession | • High power consumption<br>• Large size<br>• Expensive | • Power consumption is reduced by using Helium-3 ($He^3$) instead of Cesium in a hybrid design combining optical pumping with nuclear precession [48].<br>• Optimising Electronics for Readout Sensitivity [48].<br>• Not suitable for CubeSats due to size and power demands; used on high-end ground or airborne systems [48]. | • Not CubeSat-compatible<br>• Used in airborne magnetic anomaly detection systems (e.g., submarine detection) [48]. |
| MEMS-based | • Time-varying bias caused by temperature, current, and proximity to metallic components (hard- and soft-iron distortion) [49].<br>• Lack of reliable pre-launch compensation [49].<br>• Susceptibility to environmental disturbances [49].<br>• Sensitive to environmental disturbances during testing [49]. | • Use of Helmholtz cage for clean field simulation, helping to minimize ground disturbances [49].<br>• Compact PCB-integrated ADCS design [49]. | • Tested with SNUGLITE-I CubeSat engineering model in ground-based HILS; no confirmed CubeSat missions yet [49]. |

$$V_A = K_M B_x + V_{off} \tag{13}$$

where $K_M$ is the magnetic sensitivity of each bridge (in mV/G), $B_x$ is the magnetic field measured by bridge A (in G), and $V_{off}$ is the bridge offset voltage (in mV). Based on the HMC1053 datasheet and interpolated values for a 5 V supply, $V_{off}$ ranges between 18.75 mV and 37.5 mV. Substituting these into the characteristic Eq. (14) yields the typical, maximum, and minimum output voltage ranges for the sensor [28], resulting in $V_{A\_Max}$ and $V_{A\_Min}$ ranging from 31.25 mV to 50 mV for a typical magnetic field of 0.62 G (the approximate geomagnetic field strength in LEO). Eqs. (14) thus define the anticipated voltage outputs of the Wheatstone bridges under nominal, minimum, and maximum magnetic field exposure. However, this voltage range is relatively narrow and insufficient for direct digital conversion via the onboard ADC, which operates over a 0–2.5 V input window. To bridge this gap, the analogue signal is amplified and offset-adjusted using an instrumentation amplifier, ensuring full-scale utilisation of the ADC and improved resolution in downstream attitude processing.

$$\begin{aligned} V_{A\_Max} &= K_{M\_Max} B_{x\_Max} + V_{off\_Max} \\ V_{A\_Typ} &= K_{M\_Typ} B_{x\_Typ} + V_{off\_Typ} \\ V_{A\_Min} &= K_{M\_Min} B_{x\_Min} + V_{off\_Min} \end{aligned} \tag{14}$$

To condition the HMC1053 output for the onboard Analog-to-Digital Converter (ADC), which operates between 0 V and 2.5 V, an instrumentation amplifier (AD623) is used. The output of the amplifier for the X-axis is given by [28]:

$$MAGN_X = V_A A_D + V_{REF} \tag{15}$$

where $A_D$ is the differential gain and $V_{REF}$ is the offset voltage of the amplifier. To map the HMC1053 output range to the ADC input range, the following conditions are applied [28]:

$$\begin{aligned} V_A = V_{A\_Min} &\rightarrow MAGN_X = 0 \\ V_A = V_{A\_Max} &\rightarrow MAGN_X = 2.5V \end{aligned} \tag{16}$$

By rearranging the equations, we have:

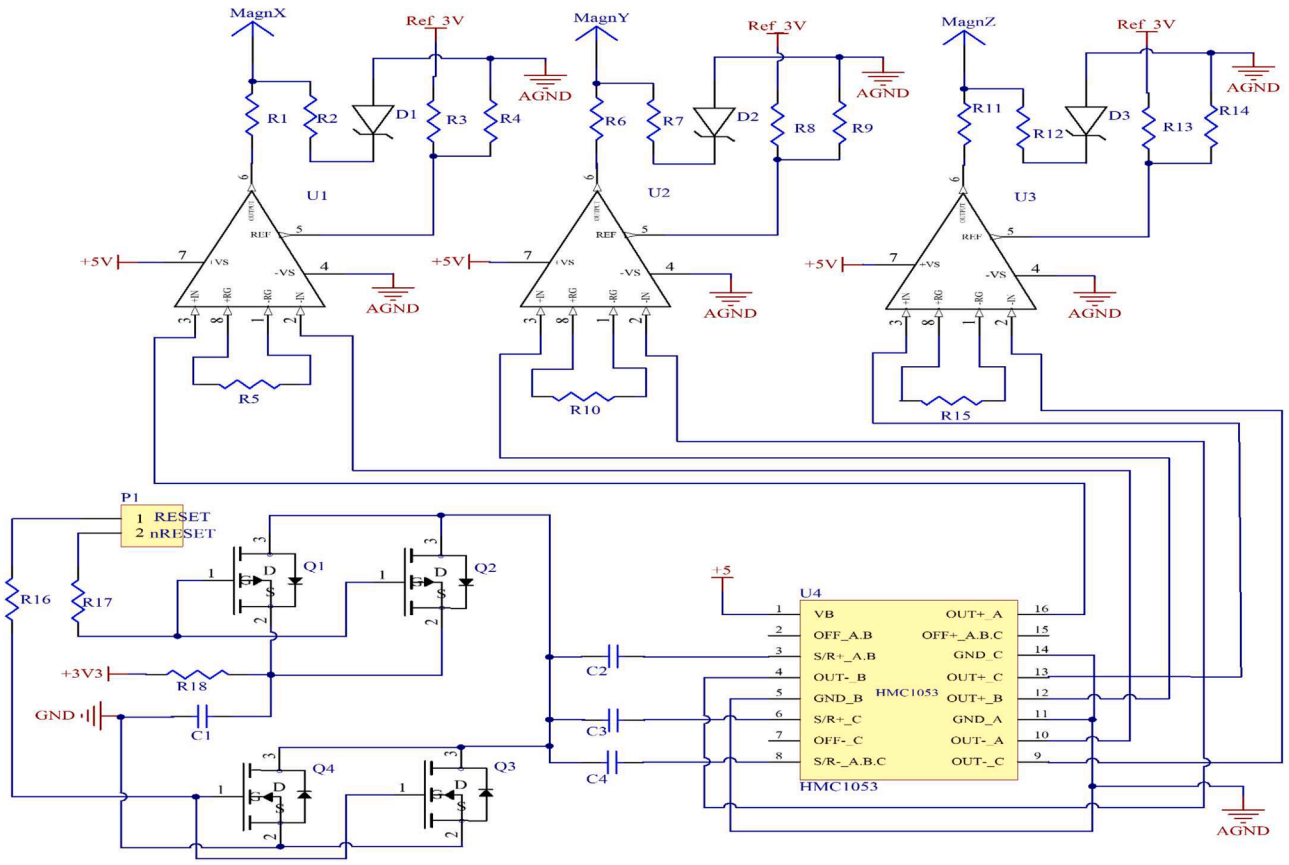


**Fig. 11.** The Magnetometer subsystem schematic.

$$\begin{aligned} A_D(-50\text{mV}) + V_{REF} &= 0 \\ A_D(-31.25\text{mV}) + V_{REF} &= 2.5\text{V} \end{aligned} \tag{17}$$

Solving these conditions yields a differential gain ($A_D = 30.77$) and an offset voltage ($V_{REF} = 1.538$ V). These values ensure that the weakest and strongest expected sensor signals are properly scaled to span the full ADC input range, maximising resolution and minimising quantisation error. To implement this gain practically, three equal external resistors ($R_5$), ($R_{10}$), and ($R_{15}$), are used in the AD623 amplifier circuit, as governed by the standard gain equation [28]:

$$A_D = 1 + \frac{100\text{k}\Omega}{R_G} \tag{18}$$

$$R_5 = R_{10} = R_{15} = \frac{100\text{k}\Omega}{A_D - 1} = 3.3\ \text{k}\Omega \tag{19}$$

Standard 3.3 kΩ resistors (1 % tolerance) are used, resulting in a slightly higher gain of AD = 31.3. This minor deviation remains within acceptable design tolerances, preserving compatibility with the ADC's input voltage range while also simplifying component selection and procurement [28].

The offset voltage $V_{REF}$ of 1.5 V is derived using a voltage divider composed of equal value resistors $R_3 - R_4$, $R_8 - R_9$, $R_{13} - R_{14}$ (1 kΩ, ±1 % tolerance) as depicted in Fig 11. The expected reference voltage output is calculated as [28]:

$$V_{REF} = \text{REF\_3V}\frac{R_4}{R_3 + R_4} = 1.5\ \text{V} \tag{20}$$

Given the slight deviation between the realised reference voltage and the theoretical target, the magnetometer's conditioned output can exhibit three distinct dynamic behaviours depending on the sensor's operating condition, whether it is functioning under typical, maximum, or minimum performance scenarios. Based on the characterised sensitivities and offset voltages, the theoretical output voltage ranges for the X-axis are determined as follows [28]:

$$\begin{aligned} \textit{Typical}\ \text{Case} \rightarrow \text{MAGN}_{X\_Typ} &= [0.894 - 1.52]\ \text{V} \\ \text{Maximum Case} \rightarrow \text{MAGN}_{X\_Max} &= [1.7 - 2.8]\ \text{V} \\ \text{Minimum Case} \rightarrow \text{MAGN}_{X\_Min} &= [-0.065 - 0.72]\ \text{V} \end{aligned} \tag{21}$$

These values ensure that the conditioned analogue output remains traceable to the actual magnetic field strength under a wide range of orbital and thermal conditions. They also guide the ADC input scaling and saturation avoidance strategy during dynamic mission phases such as eclipse or attitude manoeuvres.

The hexagonal geometry of the satellite plays a critical role in defining the spatial placement of the magnetometers, enabling comprehensive measurement of the magnetic field in three dimensions. As outlined in Table 7, the HPMAST configuration includes two HMC1053 sensors along the X-axis, two along the Y-axis, and four along the Z-axis. These sensors are symmetrically distributed across the six lateral facets of the satellite to ensure full directional coverage and increase system robustness against single-sensor anomalies. This layout leverages the structural symmetry of the hexagonal design to enhance measurement diversity and improve the accuracy of geomagnetic vector estimation under dynamic orbital conditions.

To convert the magnetometer readings from the sensor's local frame to the spacecraft's global coordinate system, a 3 × 3 transformation matrix is applied. This matrix corrects for misalignments, rotations, and scaling factors:

$$\begin{vmatrix} V_A \\ V_B \\ V_C \end{vmatrix} = \begin{vmatrix} M_{11} & M_{12} & M_{13} \\ M_{21} & M_{22} & M_{23} \\ M_{31} & M_{32} & M_{33} \end{vmatrix} X \left| \begin{pmatrix} X_{nc} \\ Y_{nc} \\ Z_{nc} \end{pmatrix} - \begin{pmatrix} B(x) \\ B(y) \\ B(z) \end{pmatrix} \right| \tag{22}$$

Where, [$X_{nc}$, $Y_{nc}$ and $Z_{nc}$] are the non-calibrated magnetic field

components, and [$B_x$, $B_y$, $B_z$] are the bias offsets for each axis.

This transformation is applied in software as part of the onboard data processing pipeline before fusing the magnetic measurements with other attitude sensors such as the gyroscope and sun sensor.

### 4.3. Gyroscope

For the HPMAST platform, a MEMS gyroscope is selected to meet the demands of compactness, low power consumption, and seamless PCB integration. The ADXRS645 is chosen for its high mechanical robustness, shock survivability up to 10,000 g, and wide operating temperature range (−40 °C to +175 °C), making it well suited for launch dynamics and the thermal environment of LEO [50]. It provides a full-scale angular rate range of ±2000°/s, extendable to ±5000°/s using an external resistor [50], with a noise density of approximately 0.25°/s/$\sqrt{\text{Hz}}$ and adequate bias stability for short-term inertial propagation, especially for yaw-axis measurements in the HPMAST attitude control system [50].

Two ADXRS645 units are mounted along the Z-axis to provide dedicated yaw-axis angular velocity measurements, particularly important during eclipse or magnetically quiet periods when magnetometer and sun sensor observability is reduced. An additional two gyroscopes are placed along the Y-axis to enhance pitch-axis estimation and improve attitude observability in fast slewing maneuvers. Each gyroscope's analogue output is connected to the onboard ADC via a low-pass filtered signal path, consisting of a 3.3 kΩ series resistor and a 22 nF shunt capacitor forming a second-order RC filter with a 3 dB bandwidth of approximately 2.2 kHz, as recommended in the datasheet [50]. This filtering, as recommended in the datasheet, attenuates demodulation noise from the sensor's internal 18 kHz resonance, ensuring cleaner signal acquisition [50]. The dual-gyroscope arrangement on each axis supports signal averaging and cross-verification, which helps mitigate individual sensor drift and enhances measurement accuracy without exceeding the platform's strict volume and power constraints. The sensor's compact 8 mm × 9 mm × 3 mm ceramic DIP package [50] supports seamless embedding into the internal PCB structure of the hexagonal tile, while its 5 V radiometric output aligns well with the ADC's input reference levels.

This integration strategy enhances both the reliability and precision of HPMAST attitude determination, especially during fast slewing or eclipse conditions, while maintaining full compliance with the platform's modular and fault-tolerant design philosophy.

### 4.4. Design discussion and analysis

Compared to the CubePMT ADCS architecture reported in [28], the proposed HPMAST design implements targeted sensor-level refinements that enhance system-level performance. Both architectures employ AMR-based magnetometers with set/reset circuitry; however, HPMAST integrates 3-axis magnetic sensor (HMC1053), while the CubePMT magnetic sensor (HMC1002) is sensing magnetic field in 2-axis. Both sensors using instrumentation amplifier (AD623), to interface with the microcontroller enabling full-scale utilization of the ADC input range (0–2.5 V). This approach not only improves resolution but also reduces PCB routing complexity.

Unlike CubePMT's partial-panel sun sensor placement, HPMAST employs a fully distributed sun sensor configuration across all six hexagonal tile faces, ensuring continuous solar vector availability during attitude manoeuvres and eclipse transitions. This maximizes observability and reduces estimation uncertainty under variable illumination conditions.

Moreover, CubePMT lacks dedicated high-rate inertial sensing, relying primarily on the fusion of low-frequency magnetometer and sun sensor data. HPMAST addresses this limitation by integrating MEMS gyroscopes (ADXRS645) with ±2000°/s range [50] and embedded PCB mounting, providing high-bandwidth angular rate data critical for rapid attitude propagation and closed-loop control, especially when external references are temporarily unavailable.

Finally, the hexagonal distribution strategy in HPMAST enhances spatial diversity and redundancy, enabling multi-axis estimation with simplified calibration compared to CubePMT's planar configurations. These integrated design decisions collectively improve attitude solution accuracy, estimation robustness, and operational agility, demonstrating the practical benefits of HPMAST's modular, fault-tolerant architecture for advanced nanosatellite missions.

## 5. Attitude actuation subsystem (Magnetorquer)

HPMAST integrates planar magnetorquers directly into four PCB layers (layers 2 to 5) as shown in Fig. 12, forming a compact and embedded actuation system that reduces volume, eliminates external wiring, and enhances both reliability and thermal control. Each coil contains 100 copper turns arranged in a square spiral geometry with external dimensions of 150 mm × 150 mm and internal spacing of 50 mm × 50 mm, as illustrated in Fig. 12. This layout is optimized to balance magnetic moment generation with Joule heating within the constrained surface area. Six magnetorquer units are symmetrically distributed on the layers (2–5) in a 4 × 6 hybrid configuration to provide full 3-axis control and redundancy.

The average length of a single square turn side is determined based on the external and internal dimensions of the coil, as shown in Eq. (23). This value is subsequently used to calculate the perimeter of each turn.

$$L_{avg} = \frac{L_{ext} + L_{int}}{2} \tag{23}$$

The total trace length for the 100-turn coil is approximately 40 m, calculated by multiplying the perimeter of a single square turn by the number of turns:

$$L_{tot} = N{\cdot}4{\cdot}L_{avg} \tag{24}$$

Where, $L_{tot}$ is the total trace length, $N$ Number of turns (100), $L_{avg}$ is the Average side length of one turn (0.1 m).

The cross-sectional area of the copper trace is 1.05 $\times 10^{-8}$ $m^2$ given by:

$$A = w{\cdot}t = 0.0003 \cdot 0.000035 \tag{25}$$

Where, $w$= 0.3 mm is trace width and $t$ =35 $\mu$m is trace thickness. The coil resistance is calculated using copper resistivity:

$$R = \frac{(\rho{\cdot}L_{tot})}{A} \approx 67.43\Omega \tag{26}$$

R quantifies the electrical resistance of the coil configuration. The coil current under a specified supply voltage (28 V from the main bus) is:

$$I = \frac{V}{R} = \frac{28}{67.43} \approx 0.415\ A \tag{27}$$

This current is used to estimate the magnetic moment and temperature. The magnetic dipole moment is computed based on the sensed current using the INA138 shunt monitor [33], following the principle:

$$m = N{\cdot}I{\cdot}A \tag{28}$$

Where, N is the number of turns, $I$ is the coil current, $A$ is the area vector perpendicular to the coil plane. This dipole interacts with the Earth's magnetic field typically approximated as $B$ = 45 $\mu$T in LEO to produce a control torque [20,28,51–55],:

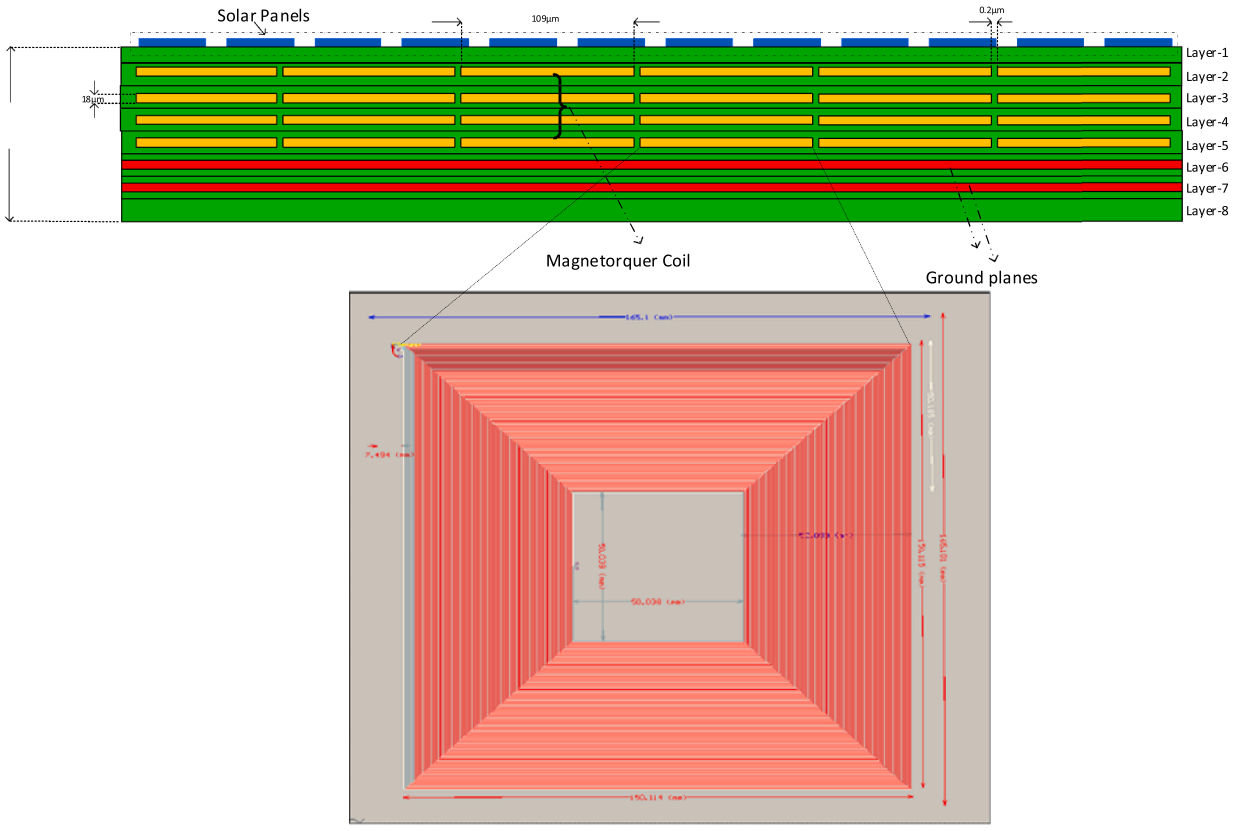


**Fig. 12.** Single coil PCB in Altium designer with dimensions.

$$\vec{\tau} = \vec{B} * \vec{m} \tag{29}$$

Where $\vec{\tau}$ is the resulting torque vector, $\vec{m}$[1] is the magnetic moment vector, and $\vec{B}$ represents the geomagnetic field vector. As illustrated in Fig. 13, an electric current flowing through the coiled conductor produces a magnetic moment ($m$) perpendicular to the coil's plane, which interacts with the Earth's magnetic field ($B$), to generate a torque ($\tau$), enabling precise attitude adjustments.

Actuation control is performed using an A4950 full-bridge DMOS motor driver, which receives PWM signals from the central MSP430 controller. This driver supports bidirectional control of the coil through logic-level inputs and includes advanced features such as internal current limiting, thermal shutdown, and under-voltage lockout. The combination of PWM-based modulation and low-resistance output transistors ensures efficient magnetic actuation with minimal switching losses, making it highly suitable for embedded CubeSat systems [51].

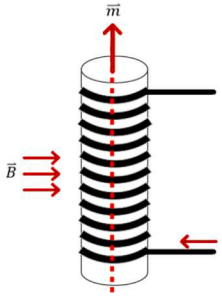


**Fig. 13.** Mathematical Modelling of Magnetorquer Coil.

To enhance functional flexibility and thermal adaptability, the embedded magnetorquer is divided into Six identical sub-coils. These sub-coils can be selectively connected in either series, parallel, or hybrid configurations via zero-ohm jumpers (SWi) [28]. This flexibility enables adaptive adjustment of torque versus power dissipation. A parallel setup delivers a higher magnetic moment, but at the cost of increased current draw and higher power consumption, while a series configuration operates at lower power, mitigating thermal impact [28]. This reconfigurability supports adaptation to mission-specific torque and thermal requirements.

The embedded coil structure inherently generates heat due to Joule losses, particularly under continuous high-current operation. The thermal behavior is modelled analytically using Stefan–Boltzmann's law for radiative dissipation:

$$T = \left(\frac{P_d + \varepsilon_I \sigma T_1^4 S}{\varepsilon_0 \sigma S}\right)^{\frac{1}{4}} \tag{30}$$

Where, $P_d = I^2 * R$ is the power dissipated in the coil, $\varepsilon$ is surface emissivity, $\sigma$ is the Stefan–Boltzmann constant, $S$ the radiative surface area. The model demonstrates a direct dependency between current level and surface temperature, confirming the need to balance torque demands with thermal constraints [28].

The torque-to-power ratio, a critical performance metric, is improved by maximizing the magnetic moment while minimizing resistive losses [51,53,55],:

[1] Different notations are used for magnetic moment in the literature, such as $\vec{D}$ [20],[28],[53],[54] and $\vec{m}$ [51],[52],[55]. This work adopts the standard symbol $\vec{m}$ for clarity and consistency in ADCS modelling, aligning with conventional physics usage.

$$\frac{\tau}{P} = \frac{\left|\vec{B} * \vec{m}\right|}{I^2 * R} \tag{31}$$

This ratio guides the selection of trace dimensions and the number of layers. Optimized designs favor a balance between a high dipole moment and manageable heat dissipation.

Finally, the time required to rotate the satellite through a certain angle $\theta$ under torque $\tau$ is approximated by [53,54,56],:

$$T = \sqrt{\frac{2J\theta}{\tau}} \tag{32}$$

Where $J$ is a moment of inertia of the satellite and $\theta$ is the desired rotation angle in radians. This relationship emphasizes the importance of achieving higher torque values, especially in detumbling scenarios.

Simulation results in similar configurations show that the temperature rise is strongly dependent on current and connection topology. Table 9 summarizes the key electrical, magnetic, and thermal parameters calculated for the hexagonal magnetorquer configuration.

In embedded magnetorquer designs, the electrical configuration of the coils plays a vital role in determining key performance indicators such as current draw, power dissipation, and magnetic dipole moment. Three connection strategies are typically explored: series, which limits current flow but increases resistance and reduces magnetic efficiency; parallel, which lowers resistance yet increases current and thermal load; and hybrid configurations, which seek a trade-off between both extremes [57].

For the HPMAST platform, various hybrid topologies such as 3 × 8, 4 × 6, 6 × 4, and 8 × 3 were simulated to evaluate their electromagnetic and thermal performance under a nominal 28 V input. Among these, the 4 × 6 hybrid configuration was selected due to its optimal balance between torque generation and thermal manageability. Unlike the denser 6 × 4 and 8 × 3 layouts that produced higher magnetic moments but resulted in excessive temperature rise, the 4 × 6 design maintained reliable operation without breaching thermal safety limits as illustrated in Fig. 14 [55].

The results, illustrated in Fig. 15, show that the hybrid layout consistently outperformed the parallel setup in thermal regulation while preserving adequate magnetic performance. Specifically, current draw in the hybrid configuration remained lower across the voltage range due to its higher equivalent resistance, which effectively mitigated Joule heating. Conversely, the parallel configuration exhibited sharp current escalation, leading to rapid heat accumulation and elevated thermal stress.

**Table 9**
Coil Specifications for the HPMAST Magnetorquer.

| Parameter | Value |
|---|---|
| Single Turn Average Length ($L_{avg}$) | 100 mm |
| Single Turn Length ($l_{turn}$) | 40 m |
| Trace Cross – sectional Area (A) | 0.0105 $mm^2$ |
| Total Area (S) | 22,500 $mm^2$ |
| Bundle Width | 30 mm |
| Copper Resistivity ($\rho$) | 1.77 × $10^{-8}$ Ω·m |
| Coil Resistance (R) | 67.43 Ω |
| Current (I) | 0.4153 A |
| Trace Width | 0.3 mm |
| Space Between Traces | 0.2 mm |
| Space Occupied by Single Trace | 0.5 mm |
| Space Available for All Traces | 50 mm |
| Number of Traces | 100 |
| Magnetic field (B) | 45 $\mu$TB |
| Magnetic moment of the single coil (m) | 0.415 $A{\cdot}m^2$ |
| Magnetorque of the single coil ($\tau$) | 18.7 $\mu N{\cdot}m$ |
| Stefan – Boltzmann constant ($\sigma$) | 5.67 × $10^{-8}$ $(Wm^2K^{-4})$ |
| Emissivity ($\varepsilon_0 = \varepsilon_1$) | 0.9 |
| Ambient temperature ($T_a$) | 298.14 K |
| $\varepsilon_0\sigma S$ | 8.18 × $10^{-9}$ $W{\cdot}m^{-2}{\cdot}K^{-4}$ |

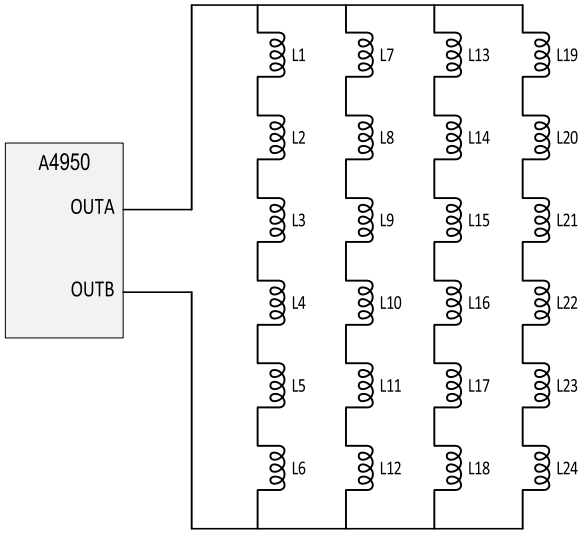


**Fig. 14.** 4 × 6 Hybrid Coil Configuration Driven by A3953 H-Bridge.

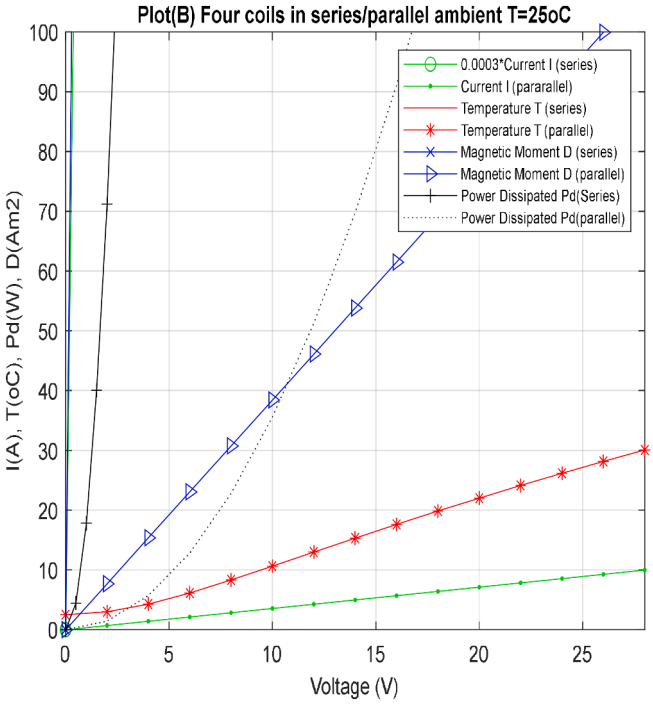


**Fig. 15.** Performance comparison of 4 × 6 hybrid and parallel coil configurations at 25 °C.

The design achieved a sustained magnetic dipole moment exceeding 0.415 A·$m^2$ and torque of approximately 18.7 μNm, while maintaining surface temperatures within safe limits (~72 °C). This balance between magnetic performance and thermal safety highlights the suitability of the hybrid configuration for embedded PCB-based actuation, where thermal management is critical.

Compared to the prior embedded coil designs in [56], as summarized in Table 10, which achieved lower dipole moments (~0.08–0.10 A·$m^2$) and similar or slightly lower peak temperatures (~70 °C), the HPMAST magnetorquer demonstrates superior magnetic output and torque capability, enabled by the adoption of uniform trace widths, maximized turn density, and a hybrid electrical topology that reduces current draw and Joule heating.

**Table 10**
Comparative Performance and Integration Metrics of HPMAST Magnetorquer vs. Reference [53].

| Parameter | HPMAST Design | Reference [53] | Key Advantage for HPMAST |
|---|---|---|---|
| **Configuration** | Hybrid (4 × 6) topology | Parallel (1 × 4), Series, or Hybrid | Hybrid selected for balance of torque and temperature |
| **Dipole Moment ($Am^2$)** | ~0.415 $Am^2$ (single coil) | ~ 0.08 – 0.10 $Am^2$ (single coil) | Increased dipole moment per unit coil |
| **Torque (μNm)** | ~18.7 μNm (single coil) | ~ 4.1 – 5.1 μNm (single coil) | Generates higher torque under typical operating current |
| **Temperature Rise ( °C)** | ~72 °C (hybrid 4 × 6 config.) | ~34–38 °C (single coil), ~70 °C (parallel config.) | Comparable thermal performance despite higher dipole and torque |
| **Integration Strategy** | Embedded within 8-layer EPS-ADCS tile with co-located drivers and sensors | Embedded within PCB layers with reconfigurable driver circuit | Full integration with EPS and ADCS enhances system-level compactness |

## 6. Future work

While the current HPMAST design successfully integrates power management and attitude control functionalities within a modular CubeSat architecture, several research directions remain open to further enhance its performance, adaptability, and impact:

Future studies may investigate potential enhancements in the embedded magnetorquer design, including optimizing geometric parameters, electrical configurations, and material selections. These improvements aim to increase magnetic dipole moments while reducing power dissipation and thermal impact, supporting agile attitude control and ensuring compatibility with CubeSat operational constraints. At the platform level, advanced thermal management solutions, such as Smart Radiator Devices (SRDs), could be explored to improve heat rejection from high-density subsystems, thereby enhancing overall thermal stability and operational reliability in compact nanosatellite architectures [58].

Recent studies have demonstrated the effectiveness of hybrid metaheuristic algorithms, such as Sine Cosine Optimization combined with Balloon Effect (SCO + BE), in achieving robust and adaptive load frequency control in microgrids under dynamic conditions [59]. Although previously applied in high-voltage terrestrial systems, these optimization frameworks could be adapted for embedded satellite subsystems. Future research may explore the application of SCO + BE techniques to optimize HPMAST's power conditioning and distribution strategies, enhancing system efficiency, reliability, and thermal safety under orbital conditions.

Additionally, empirical analyses [60] have underscored how technical assistance and spatial spillover effects can accelerate energy access and drive technological development in low-resource regions. While HPMAST is designed as a modular satellite tile for nanosatellite missions, its compact architecture could be repurposed for development-focused applications. For example, future work may explore deploying HPMAST-based small satellite constellations for remote electrification monitoring, distributed IoT sensing, or communication relay services in underdeveloped regions, thereby providing targeted technical assistance and advancing global energy equity goals.

Collectively, these directions will build upon the HPMAST platform's foundation to enable its adoption in broader aerospace and societal applications.

## 7. Conclusion

This paper presented the design, modelling, and implementation of HPMAST, a compact Hexagonal Power Management and Attitude Sensor Tile tailored for modular nanosatellite platforms. The HPMAST integrates solar energy harvesting with hysteresis-based MPPT boost conversion achieving a regulated 28 V output at 93 % peak efficiency, alongside multi-rail power distribution and a distributed attitude determination subsystem comprising sun sensors, AMR magnetometers, and MEMS gyroscopes embedded within an eight-layer PCB architecture.

The embedded planar magnetorquer demonstrated a magnetic dipole moment of approximately 0.415 $A{\cdot}m^2$ while maintaining safe thermal operating margins, enabling effective three-axis actuation essential for agile CubeSat operations. By leveraging carefully selected COTS components optimized for efficiency and power loss, the HPMAST achieves a minimal footprint, reduced cost, and enhanced energy efficiency. Its modular and distributed design supports scalable, fault-tolerant satellite architectures, enabling autonomous operation across multiple faces while optimizing thermal dissipation and payload accommodation.

Overall, the HPMAST concept demonstrates a practical, integrated solution to enhance power conditioning, distribution, and attitude control functionalities in next-generation nanosatellites requiring compact, reconfigurable, and energy-efficient subsystems.

## CRediT authorship contribution statement

**Zainab Mousawi:** Writing – original draft, Visualization, Validation, Methodology, Investigation, Formal analysis, Data curation, Conceptualization. **Anwar Ali:** Writing – original draft, Supervision, Resources, Methodology, Investigation, Formal analysis, Conceptualization. **Muhammad Rizwan Mughal:** Writing – original draft, Supervision, Methodology, Conceptualization. **Shoaib Ahmed Khan:** Writing – original draft, Visualization, Methodology, Formal analysis, Conceptualization. **Augustine Egwebe:** Writing – original draft, Validation, Supervision, Resources.

## Declaration of competing interest

On behalf of all authors, the corresponding author declares here that there is no conflict of interest concerning the publication of this article.

## Data availability

No data was used for the research described in the article.

## References

[1] E. Koktas, E. Basar, Communications for the Planet Mars: past, present, and future, IEEE Aerosp. Electron. Syst. Mag. 39 (9) (2024) 216–258, https://doi.org/10.1109/MAES.2024.3396117.
[2] J. Puig-Suari and C. Turner, "Development of the standard CubeSat deployer and a CubeSat class PicoSatellitel".
[3] H. Heidt, J.Puig-Suari, A.S.Moore, S.Nakasuka, and R.J.Twiggs, "Heidt SSC00-V-5 CubeSat: a new generation of picosatellite for education and industry low-cost space experimentation".
[4] O.A. Asiyanbola, et al., An analytical outlook of the commercial space industry for the last frontier: potential entrepreneurial evaluation of the African space sector, New Sp 9 (3) (2021) 169–186, https://doi.org/10.1089/space.2020.0016.
[5] H.J. Kramer, A.P. Cracknell, An Overview of Small Satellites in Remote Sensing, Taylor and Francis Ltd, 2008, https://doi.org/10.1080/01431160801914952.
[6] M.N. Sweeting, Modern small satellites-changing the economics of space, Proc. IEEE 106 (3) (2018) 343–361, https://doi.org/10.1109/JPROC.2018.2806218.
[7] W. Lamine, A. Anderson, S.L. Jack, A. Fayolle, Entrepreneurial space and the freedom for entrepreneurship: institutional settings, policy, and action in the space industry, Strateg. Entrep. J. 15 (2) (2021) 309–340, https://doi.org/10.1002/sej.1392.
[8] A. Gaga, O. Diouri, M.Ouazzani Jamil, Design and realization of nano satellite cube for high precision atmosphere measurement, Results Eng 14 (2022) 100406, https://doi.org/10.1016/j.rineng.2022.100406.

[9] T. Saeidi, S. Karamzadeh, Enhancing CubeSat Communication Through Beam-Steering Antennas: a Review of Technologies and Challenges, Multidisciplinary Digital Publishing Institute (MDPI), 2025, https://doi.org/10.3390/electronics14040754.

[10] S. Lu, et al., A Survey on CubeSat Missions and Their Antenna Designs, MDPI, 2022, https://doi.org/10.3390/electronics11132021.

[11] L. Schirone, M. Ferrara, P. Granello, C. Paris, and F. Pellitteri, "Power bus management techniques for space missions in low earth orbit," 2021, MDPI. doi: 10.3390/en14237932.

[12] A. Ali, M.R. Mughal, S.A. Khan, K.S. Teng, Thermal modeling and empirical verification of multi unit small satellites, Results Eng 25 (November 2024) (2025) 104217, https://doi.org/10.1016/j.rineng.2025.104217.

[13] U. Shakoor, M. Alayedi, E.E. Elsayed, Comprehensive analysis of Cubesat electrical power systems for efficient energy management, Discov. Energy 5 (1) (2025), https://doi.org/10.1007/s43937-025-00069-5.

[14] R.A. Deepak and R.J. Twiggs, "Thinking out of the box: space science beyond the CubeSat." [Online]. Available: www.JoSSonline.com.

[15] H. Djojodihardjo, Structural Integrity of Spacecraft Structures Subject to motion, Thermo-Structural Dynamics and Environmental Effects - an overview, Elsevier Ltd, 2024, https://doi.org/10.1016/j.actaastro.2024.05.034.

[16] L.M. Reyneri et al., *9 Design solutions for modular satellite architectures*. [Online]. Available: www.intechopen.com.

[17] A. Ali, S.A. Khan, M.U. Khan, H. Ali, and M.R. Mughal, "Design of modular power management and attitude control subsystems for a microsatellite," vol. 2018, 2018, doi: 10.1155/2018/2515036.

[18] O. Abolghasemi, H. Soleimani, S.H. Sedighy, Scalable solutions for implementing satellite-based sensor networks, Results Eng 23 (June) (2024) 102481, https://doi.org/10.1016/j.rineng.2024.102481.

[19] S.A. Khan, A. Ali, M. Tahir, Z. Tao, Efficient power conditioning: enhancing electric supply for small satellite missions, Aerospace 11 (11) (2024), https://doi.org/10.3390/aerospace11110920.

[20] M.R. Ali, A., Reyneri, L., De Los Rios, J.C., Ali, H., & Mughal, *2012 15th International Multitopic Conference*. IEEE. [Online]. Available: doi: 10.1109/INMIC.2012.6511478.

[21] B. Hussein, G.S. Member, Centralized, distributed, and module-integrated electric power system schemes in CubeSats : performance assessment, IEEE Access 10 (2022) 55396–55407, https://doi.org/10.1109/ACCESS.2022.3176902.

[22] F. Josue et al., "applied sciences model-based design and testbed for CubeSat attitude determination and control system with magnetic actuation," 2024.

[23] Low cost triple-junction solar cell for space applications (CTJ-LC) [Online]. Available: www.cesi.it, 2020.

[24] L.M. Shaker, A.A. Al Amiery, M.M. Hanoon, W.K. Al Azzawi, Examining the influence of thermal effects on solar cells : a comprehensive review, Sustain. Energy Res. (2024), https://doi.org/10.1186/s40807-024-00100-8.

[25] G. Vieira, M.U. De Ara, M. Dhimish, and M.I.S. Guerra, "A comprehensive review on bypass diode application on photovoltaic modules," pp. 1–21, 2020.

[26] A. Ali, L.M. Reyneri, J. Carlos De Los Rios, and M.Rizwan Mughal, "Components selection for a simple boost converter on the basis of power loss analysis".

[27] R. Ravindran, A.M. Massoud, State-of-the-Art DC-DC Converters for Satellite Applications: a Comprehensive Review, Multidisciplinary Digital Publishing Institute (MDPI), 2025, https://doi.org/10.3390/aerospace12020097.

[28] A. Ali, M.R. Mughal, H. Ali, L. Reyneri, Innovative power management, attitude determination and control tile for CubeSat standard NanoSatellites, Acta Astronaut 96 (1) (2014) 116–127, https://doi.org/10.1016/j.actaastro.2013.11.013.

[29] T. Piovesan, H.C. Sartori, J.E. Baggio, and J.Renes Pinheiro, "CubeSat electrical power supplies optimization-comparison between conventional and optimal design methodology".

[30] B.V. Nexperia, GAN3R2-100CBE: 100 V, 3.2 Mohm Gallium Nitride (GaN) FET in a 3.5 Mm x 2.13 Mm Wafer Level Chip-Scale Package (WLCSP) [Product Data Sheet], April 27, Nexperia, 2023, https://www.nexperia.com/products/gan-fets/GAN3R2-100CBE.html.

[31] L. Technology Corporation, "LT1017/LT1018 - micropower dual comparator." [Online]. Available: http://www.linear.com/leadfree/.

[32] I.U. Zaman, A. Eltawil, S. Member, O. Boyraz, Wireless communication technologies in omnidirectional CubeSat crosslink : feasibility study and performance analysis, IEEE J. Miniaturization Air Sp. Syst. 2 (3) (2021) 157–166, https://doi.org/10.1109/JMASS.2021.3079102.

[33] Texas Instruments. (n.d.). INA138 low- and high-side current shunt monitor data sheet [Data sheet]. Retrieved May 16, 2025, from https://www.ti.com/lit/ds/symlink/ina138.pdf.

[34] Texas Instruments, *MSP430F543xA Mixed-signal microcontrollers datasheet (Rev. K)*, 2018. [Online]. Available: https://www.ti.com/lit/gpn/msp430f5438a.

[35] A. Ali, H. Ali, J. Tong, M.R. Mughal, S.U. Rehman, Modular design and thermal modeling techniques for the power distribution module (PDM) of a micro satellite, IEEE Access 8 (2020) 160723–160737, https://doi.org/10.1109/ACCESS.2020.3020865.

[36] Texas Instruments, *LM2679 SIMPLE SWITCHER® 5-A step-down voltage regulator with adjustable current limit datasheet (Rev. O)*, 2016. [Online]. Available: https://www.ti.com/lit/gpn/lm2679.

[37] TPL5010 Nano-power system timer with watchdog function [Online]. Available: www.ti.com, 2015.

[38] "MCP2515 Notes." [Online]. Available: https://ww1.microchip.com/downloads/en/DeviceDoc/MCP2515-Stand-Alone-CAN-Controller-with-SPI-20001801J.pdf.

[39] SN65HVD233, Sn65hvd234, Sn65hvd235 [Online]. Available: www.ti.com, 2002.

[40] IXYS Corporation, CPC1822 Photovoltaic Module Datasheet. [Online]. Available: https://www.digikey.co.uk/en/products/detail/ixys-integrated-circuits-division/CPC1822N/1485716.

[41] P. Ripka, Review of fluxgate sensors, Sensors Actuators A Phys 33 (3) (1992) 129–141, https://doi.org/10.1016/0924-4247(92)80159-Z.

[42] H. Nhalil, et al., Planar Hall effect magnetometer with 5 pT resolution, IEEE Sensors Lett. 3 (12) (2019), https://doi.org/10.1109/LSENS.2019.2947681.

[43] J.S. Bennett, et al., Precision Magnetometers for Aerospace applications: a review, MDPI, 2021, https://doi.org/10.3390/s21165568.

[44] S. Ziegler, R.C. Woodward, H.H.C. Iu, L.J. Borle, Current sensing techniques: a review, IEEE Sens. J. 9 (4) (2009) 354–376, https://doi.org/10.1109/JSEN.2009.2013914.

[45] M.J. Haji-Sheikh, G. Morales, B. Altuncevahir, A.R. Koymen, Anisotropie magnetoresistive model for saturated sensor elements, IEEE Sens. J. 5 (6) (2005) 1258–1263, https://doi.org/10.1109/JSEN.2005.857879.

[46] Honeywell International Inc., *HMC1051/1052/1053 magnetic sensors datasheet.* [Online]. Available: https://aerospace.honeywell.com/content/dam/aerobt/en/documents/learn/products/sensors/datasheet/HMC_1051-1052-1053-B_Data_Sheet.pdf.

[47] A.P. Hoffmann, M.B. Moldwin, B.P. Strabel, L.V. Ojeda, Enabling boomless CubeSat magnetic field measurements with the quad-mag magnetometer and an improved underdetermined blind source separation algorithm, J. Geophys. Res. Sp. Phys. 128 (9) (2023), https://doi.org/10.1029/2023JA031662.

[48] L.H. Regoli, et al., Investigation of a low-cost magneto-inductive magnetometer for space science applications, Geosci. Instrumentation, Methods Data Syst. 7 (1) (2018) 129–142, https://doi.org/10.5194/gi-7-129-2018.

[49] J.E. Lenz, A review of magnetic sensors, Proceedings of the IEEE 78 (6) (1990) 973–989.

[50] Analog Devices, Inc., ADXRS645: high temperature, vibration rejecting ±2000°/sec gyroscope, Rev. [Online]. Available: https://www.analog.com/en/products/adxrs645.html.

[51] Allegro MicroSystems. (2022, March 21). A4950: full-bridge DMOS PWM motor driver (Rev. 7) [Data sheet]. https://www.allegromicro.com/-/media/files/datasheets/a4950-datasheet.pdf.

[52] H. Ali, M.R. Mughal, Q.Ul Islam, M.R. Anjum, S. Ishaq, L.M. Reyneri, Parametric optimization and analysis of power efficient magnetorquer rod actuator for nanosatellite, IEEE J. Miniaturization Air Sp. Syst. 3 (2) (2022) 30–35, https://doi.org/10.1109/JMASS.2022.3186405.

[53] H. Ali, Q.U. Islam, M.R. Mughal, R. Mahmood, M.R. Anjum, L.M. Reyneri, Design and analysis of a rectangular PCB printed magnetorquer for nanosatellites, IEEE J. Miniaturization Air Sp. Syst. 2 (3) (2021) 105–111, https://doi.org/10.1109/JMASS.2020.3029489.

[54] Z. Mukhtar, A. Ali, M.R. Mughal, L.M. Reyneri, Design and comparison of different shapes embedded magnetorquers for CubeSat standard nanosatellites, in: 2016 Int. Conf. Comput. Electron. Electr. Eng. ICE Cube 2016 - Proc, 2016, pp. 175–180, https://doi.org/10.1109/ICECUBE.2016.7495218.

[55] M.R. Mughal, H. Ali, A. Ali, J. Praks, L.M. Reyneri, Optimized design and thermal analysis of printed magnetorquer for attitude control of reconfigurable nanosatellites, IEEE Trans. Aerosp. Electron. Syst. 56 (1) (2020) 736–747, https://doi.org/10.1109/TAES.2019.2933959.

[56] S.A. Khan, A. Ali, Y. Shiyou, J. Tong, Reconfigurable asymmetric embedded magnetorquers for attitude control of nanosatellites, IEEE J. Miniaturization Air Sp. Syst. 2 (4) (2021) 236–243, https://doi.org/10.1109/JMASS.2021.3094232.

[57] A. Ali, M.R. Mughal, H. Ali, L.M. Reyneri, M.N. Aman, Design, implementation, and thermal modeling of embedded reconfigurable magnetorquer system for nanosatellites, IEEE Trans. Aerosp. Electron. Syst. 51 (4) (2015) 2669–2679, https://doi.org/10.1109/TAES.2015.130621.

[58] Y. Chen, et al., Adaptive thermal radiation design for spacecraft heat dissipation, Results Eng 27 (May) (2025) 106262, https://doi.org/10.1016/j.rineng.2025.106262.

[59] A.T. Hassan, et al., Sine cosine optimization and balloon effect for adaptive load frequency control in microgrids with consirning of controlled loads, J. Low Freq. Noise Vib. Act. Control (2025), https://doi.org/10.1177/14613484241311951.

[60] Q. Wang, J. Guo, R. Li, A. Mikhaylov, N. Moiseev, Does technical assistance alleviate energy poverty in sub-Saharan African countries? A new perspective on spatial spillover effects of technical assistance, Energy Strateg. Rev. 45 (2023), https://doi.org/10.1016/j.esr.2022.101047.